

Scaling laws for the geometry of an impact-induced magma ocean

Miki Nakajima^{1,2}, Gregor J. Golabek³, Kai Wünnemann⁴, David C. Rubie³, Christoph Burger⁵, Henry J. Melosh⁶, Seth A. Jacobson⁷, Lukas Manske⁴, and Scott D. Hull¹

¹Department of Earth and Environmental Sciences, University of Rochester, 227 Hutchison Hall, Rochester, NY 14627, USA.

²Department of Terrestrial Magnetism, Carnegie Institution for Science, 5241 Broad Branch Rd NW, Washington, DC 20015, USA.

³Bayerisches Geoinstitut, University of Bayreuth, Universitätsstrasse 30, 95440 Bayreuth, Germany.

⁴Museum für Naturkunde, Leibniz-Institut für Evolutions- und Biodiversitätsforschung, Invalidenstrasse 43, 10115 Berlin, Germany.

⁵Institute of Astronomy and Astrophysics, University of Tübingen, Auf der Morgenstelle 10, 72076 Tübingen, Germany.

⁶Department of Earth, Atmospheric and Planetary Sciences, Purdue University, 550 Stadium Mall Drive, West Lafayette, IN 47907, USA.

⁷Department of Earth and Environmental Sciences, Michigan State University, 288 Farm Lane, East Lansing, MI 48823, USA.

Abstract

Growing protoplanets experience a number of impacts during the accretion stage. A large impactor hits the surface of a protoplanet and produces a magma ocean, where the impactor's iron emulsifies and experiences metal-silicate equilibration with the mantle of the protoplanet while it descends towards the base of the magma ocean. This process repeatedly occurs and determines the chemical compositions of both mantle and core. The partitioning is controlled by parameters such as the equilibration pressure and temperature, which are often associated with or assumed to be proportional to the pressure and temperature at the base of the magma ocean. The pressure and temperature depend on both the depth and shape of a magma ocean because a spatially confined magma ocean, namely, a melt pool, can have a larger equilibrium pressure than a radially uniform (global) magma ocean even if their melt volumes are the same. Here, we develop scaling laws for (1) the total internal energy gain due to an impact, and (2) the heat distribution within the mantle based on more than 100 smoothed particle hydrodynamic (SPH) simulations. We use Legendre polynomials to describe these scaling laws and determine their coefficients by linear regression, minimizing the error between our model and SPH simulations. The input parameters are the impact angle θ (0° , 30° , 60° , and 90°), total mass M_T ($1M_{\text{Mars}} - 53M_{\text{Mars}}$, where M_{Mars} is the mass of Mars), impact velocity v_{imp} ($v_{\text{esc}} - 2v_{\text{esc}}$, where v_{esc} is the mutual escape velocity), and impactor-to-total mass ratio γ ($0.03 - 0.5$). We find that the internal energy gain by a large impact is well characterized by the summation of the kinetic energy and accretional potential energy release as a function of the impact angle. We determine that the equilibrium pressure at the base of a melt pool can be higher (by 10 – 50%) than those obtained from conventional radially-uniform global magma ocean models. This could have a significant impact on element partitioning. These melt scaling laws are publicly available on GitHub (<https://github.com/mikinakajima/MeltScalingLaw>).

Keywords: melt volume; giant impact; scaling law; magma ocean; metal-silicate equilibration

1. Introduction

Protoplanets experience numerous impacts as they accrete. These impacts have shaped the configuration of the solar system, given that the origins of the Earth-Moon system (e.g., Hartmann and Davis, 1975; Cameron and Ward, 1976), the Pluto-Charon system (e.g., McKinnon, 1988, 1989; Canup, 2005) and perhaps the Martian moons (e.g., Rosenblatt, 2011; Craddock, 2011; Citron et al., 2015; Rosenblatt et al., 2016;

Nakajima and Canup, 2017; Canup and Salmon, 2018; Hyodo et al., 2018) can be explained by a giant impact. Additionally, the large core of Mercury (e.g., Benz et al., 2007) and Uranus's axis tilt may have also been formed via a giant impact as well (e.g., Safronov, 1969; Slattery et al., 1992; Kegerreis et al., 2018).

Giant impacts are not only responsible for shaping the architecture of the planetary system, but also determine the evolving chemistry of a planet. The chemical compositions of both the mantle and core of a protoplanet evolve over time as new impactor materials are added. When an impactor hits the protoplanet (target),

Email address: mnakajima@rochester.edu (Miki Nakajima^{1,2})

the outer part of the mantle becomes molten and forms a magma ocean. If the impactor's iron core is sufficiently small enough to be emulsified and turbulently mixed (or its metallic iron was not incorporated into a core in the first place), then it will equilibrate with some fraction of the target mantle (e.g., Dahl and Stevenson, 2010; Deguen et al., 2014; Landeau et al., 2016; Lherm and Deguen, 2018). This equilibration enriches iron metal from the impactor with siderophile elements whereas lithophile elements will partition preferentially into the silicate melt. The iron continues to sink to the bottom of the magma ocean and eventually merges with the target core (e.g., Stevenson, 1990; Wade and Wood, 2005; Rubie et al., 2011, 2003, 2015). However, if the impactor's iron metal is large, it may not have time to equilibrate with the target's mantle before merging with the target's core (Dahl and Stevenson, 2010). Thus, depending on the impact scenario, the sinking iron and the magma ocean experience metal-silicate equilibration to a certain degree and potentially change the evolving chemistries of the core and mantle.

The metal-silicate partition coefficient of element i is defined as,

$$D_i^{\text{metal-sil}} = C_i^{\text{metal}} / C_i^{\text{sil}}, \quad (1)$$

where C_i^{metal} and C_i^{sil} are the concentrations of element i in metal and silicate, respectively (e.g., Rubie et al. 2015). This coefficient is a function of equilibrium temperature T_{eq} and pressure P_{eq} and of other factors such as the oxygen fugacity. Conventionally, the values of T_{eq} and P_{eq} are often associated with or assumed to be proportional to the values at the bottom of a global (radially uniform) magma ocean of equivalent volume to the melt that is generated by the impact (Figure 1a). However, an impact can produce a spatially confined melt pool (Figure 1b) (Tonks and Melosh, 1992; Rubie et al., 2015) that centers around the impact point, which would provide higher T_{eq} and P_{eq} than those of a global magma ocean while having the same melt volumes. Due to isostatic adjustment this melt pool would radially spread out and become a magma ocean with a uniform depth over time (Reese and Solomatov, 2006), however, this timescale (a rough estimate is ≈ 10 s of years for a 1000 km-sized magma ocean, see our discussion in Section 4.3) is likely to be longer than the equilibration timescale, ranging from hours (set by the turbulent mixing timescale) to months (set by the ≈ 1 cm-sized iron droplets' sinking timescale – but of course this timescale strongly depends on the viscosity). Therefore, a melt pool is likely to be more relevant.

Insightful and extensive studies have been conducted on estimating the volume of an impact-induced magma

ocean (e.g., Bjorkman and Holsapple, 1987; Tonks and Melosh, 1993; Pierazzo et al., 1997; Pierazzo and Melosh, 2000; Reese and Solomatov, 2006; Barr and Citron, 2011; Abramov et al., 2012; Monteux and Arkani-Hamed, 2019). However, some of these studies focus on head-on collisions (for which the impact angle θ is 0° ; see Figure 2 for the definition of θ) because the simulation of these impacts is numerically less expensive than those of oblique impacts, which require 3D simulations, even though oblique impacts are more likely (e.g., Shoemaker 1962; Agnor et al. 1999). Furthermore, some of the studies are based on iSALE2D, which is an extensively tested impact code (e.g., Wünnemann et al. 2006), that assumes central gravity instead of self gravity. Therefore, the scaling laws derived with the code may not accurately capture tidal heating or change in the potential energy, which can be important for large impacts, as shown in Section 3.1.2. Moreover, no analytical model is available that describes how the heat is distributed within the mantle of the target body. This renders challenging the prediction of the depth and geometry of an impact-induced melt pool.

Here, we have developed scaling laws for (1) the total internal energy gain due to a large impact, and (2) impact-induced heat distribution within the mantle. Legendre polynomials are used for the scaling laws and their coefficients are determined by linear regression to minimize the error between our model and mantle heating computed by more than 100 giant impact simulations. By using these laws combined with the initial thermal profile of a planetary body, we can predict the thermal profile of the post-impacted body. Moreover, once the criterion for melting is specified, the melt volume of a magma ocean and shape of a melt pool can be calculated.

2. Methods

2.1. Smoothed particle hydrodynamics

We use the smoothed particle hydrodynamics (SPH) method to simulate giant impacts. SPH is a Lagrangian method and has been used for representing planetary impact phenomena (e.g., Canup 2004). All the SPH particles have the same masses in our simulations. The conservation equations for mass, momentum equation, and energy are solved simultaneously. This SPH code follows the standard implementation that uses artificial viscosity to describe the shock front (see Section 4 in Monaghan, 1992). We use M-ANEOS as an equation of state (Thompson and Lauson, 1972; Melosh, 2007),

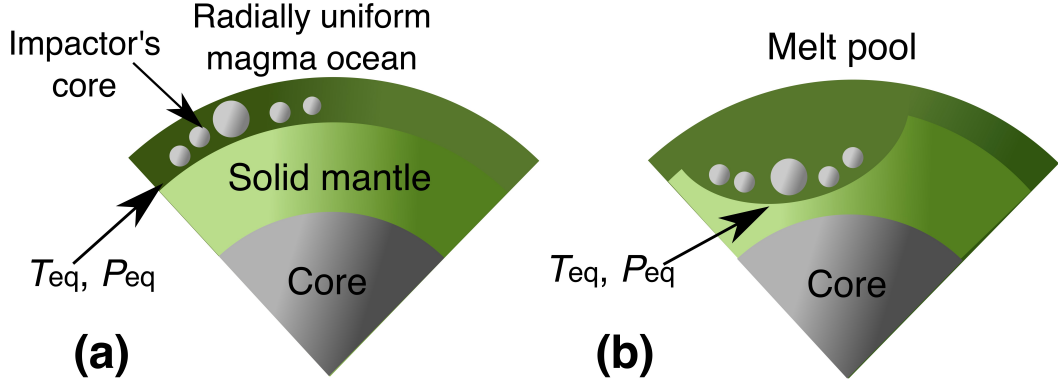


Figure 1: Schematic view of (a) a global magma ocean and (b) a regionally confined melt pool. T_{eq} and P_{eq} are the equilibrium temperatures and pressures, respectively.

which is a semi-analytic equation of state and includes phase changes. This equation of state (EOS) has been frequently used in previous impact simulations (e.g., Canup, 2004). The input parameters for M-ANEOS are listed in Supplementary Information. This version of M-ANEOS here does not include the effect of melting, and therefore it overestimates the temperature of a material that is heated above the melting point. The mantle and core are assumed to be dunite and iron, respectively. The initial mantle mass fractions f_{mantle} for an impactor and mantle are 0.7 (i.e. the core mass fraction is 0.3). Initially, the mantle and core of a body have adiabatic temperature profiles. The entropies for the mantle and core are assumed to be 3160 J/K/kg and 1500 J/K/kg, respectively, which results in approximately ≈ 2000 K near the planetary surface. Effects of varying the initial temperatures are considered in Section 3.4. The number of SPH particles in our simulations is on the order of $10^4 - 10^5$, as discussed in more detail in Section 4.6. Our SPH code does not include material strength and the implication of this omission is discussed in Section 4.4. The details of the code and settings are described in detail in our previous studies (e.g., Nakajima and Stevenson, 2014, 2015).

2.2. Parameters for the SPH simulations

The input parameters for the SPH simulations are the impact angle θ ($0 - 90^\circ$, Figure 2a), total mass M_T ($1M_{Mars} - 53M_{Mars}$, where M_{Mars} is the mass of Mars), which is the sum of target and impactor masses, the impactor-to-total-mass ratio γ (0.03–0.5), impact velocity v_{imp} ($v_{esc} - 2v_{esc}$), where v_{esc} is the mutual escape velocity ($v_{esc} = \sqrt{2G(M_t + M_i)/(R_t + R_i)}$, where M_t , M_i , R_t , R_i are the target mass, impactor mass, target radius and impactor radius). The given ranges are expected

to be common near the end of the planetary accretion stage (e.g., Ward, 1993; Agnor et al., 1999; Agnor and Asphaug, 2004), when impacts are largest and have the greatest influence on planetary composition. The impact velocity can be higher, but most of large impacts occur within the specified range, $v_{esc} - 2v_{esc}$ (e.g., Stewart and Leinhardt, 2012). The values of the employed parameters are listed in Table 1 and input parameters are listed in Tables S.1 - S.3.

3. Scaling law of mantle melt and heat distribution

The SPH results are listed in Tables S.1-S.2 for the $v_{imp} = v_{esc}$ cases and in Table S.3 for the $v_{imp} \geq 1.1v_{esc}$ cases. The run name “M” represents the same set of initial conditions with four different impact angles (in the range of $\theta = 0^\circ - 90^\circ$). ID represents a specific SPH simulation. dE is the total internal energy gain of the post-impact body, dE_{mantle}/dE represent the fraction of the internal energy partitioned into the mantle (i.e. $1 - dE_{mantle}/dE$ is the fractional energy partitioned into the core). $M_{mantle}/f_{mantle}M_T$ represents the extent of perfect or imperfect accretion (if this value is close to 1, the impactor accretes into the target almost perfectly, whereas if this value is smaller than 1, some mass does not accrete into the post-impact body). MF , MF_A , and MF_L describe the melt fractions of the post-impact body based on different melt criteria (see Section 3.1.4). L_2 refers to the L_2 norm computed when comparing an SPH simulation and our model (see Section 3.2). Additional outputs are discussed in Section S.1.2.

We describe the results of our model in terms of (1) the total internal energy gain by impact in Section 3.1

Symbol	Description	values	references
θ	Impact angle	$0-90^\circ$	
M_T	Total mass	$1 - 53 M_{\text{Mars}}$	
γ	Impactor-to-total-mass ratio	$0.03 - 0.5$	
M_{Mars}	Martian mass	$6.39 \times 10^{23} \text{ kg}$	
M_t	Target mass	$(1 - \gamma)M_T$	
M_i	Impactor mass	γM_T	
R_t	Target radius	$1 - 3R_{\text{Mars}}$	
R_i	Impactor radius	$0.5 - 1.5R_{\text{Mars}}$	
R	Radius of a planet whose mass is $M_t + M_i$	$1 - 3R_{\text{Mars}}$	
v_{imp}	Impact velocity	$v_{\text{esc}} - 2 v_{\text{esc}}$	
v_{esc}	Mutual escape velocity	$4.2 - 17.5 \text{ km/s}$	
M_{mantle}	Post-impact Mantle mass	$0.5 - 1.0$	
h	Mantle heating/total heating	$0.7 - 1.0$	
L	Latent heat	$7.18 \times 10^5 \text{ J/kg}$	1
E_M	Specific energy for melting	$5.2 \times 10^6 \text{ J/kg}$	2
ΔE	Internal energy gain	$10^{29} - 10^{32} \text{ J}$	3
KE_0	Kinetic energy		4
ΔPE	Change in potential energy		5
c_v	Specific heat	1000 J/K/kg	6
f_{mantle}	Initial mantle mass fraction	0.7	
dE_{mantle}/dE	Fractional heating of mantle	$0.6-1$	

Table 1: List of important parameters used in this paper. 1: Navrotsky (1995), 2: Pierazzo et al. (1997), 3: Equation 4, 4: Equation 2, 5: Equation 3, 6: Estimated from M-ANEOS.

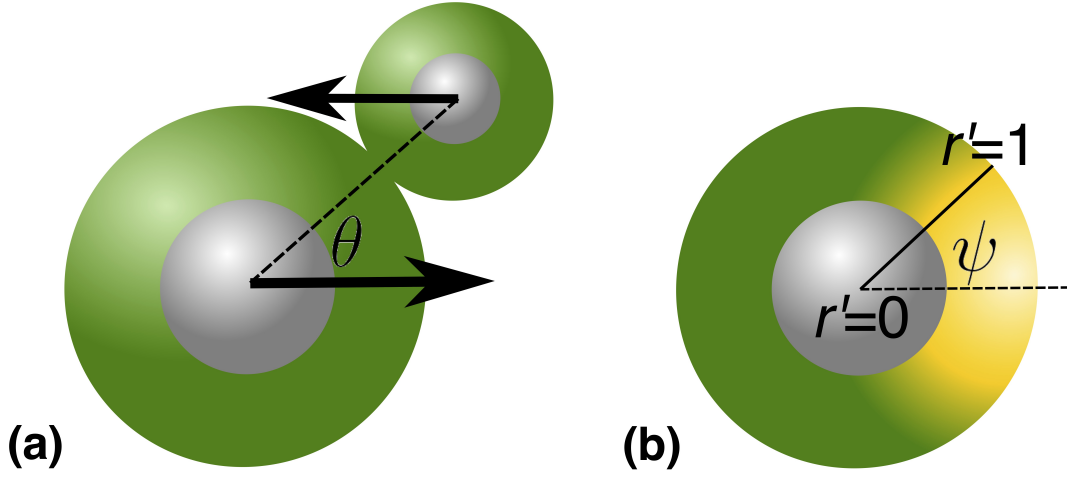


Figure 2: Definition of our model parameters. (a) θ is the impact angle, where the arrows indicate the directions of motions of both the impactor and the target. (b) The polar angle ψ is defined to be zero where the shock-heating is most significant, which is typically close to the impact point. The heat distribution is symmetric along the $\psi = 0$ axis. r' is the normalized radius (0 is the center of the body and 1 is its surface).

and (2) heat distribution within mantle in Section 3.2. By combining these two sets of results, the internal energy gain and magma ocean geometry can be modeled as discussed in Section 3.3.

3.1. Impact-induced heating

3.1.1. SPH simulations

Examples of our SPH simulations are presented in Figure 3 (model M0). The orange-red colormap displays the gain of specific internal energy of the mantle normalized by 10^5 J/kg and the grey color applies to iron. These snapshots clearly show that the internal energy gain depends on the impact angle θ . At a head-on collision ($\theta = 0^\circ$), antipodal heating is prominent due to focusing of shock waves at the opposite side of the impact point and due to deformation of the mantle. Part

of the mantle at the antipode deforms significantly and expands radially upon impact. When it falls back and hits the core mantle boundary, the potential energy is converted into internal energy of the mantle. This effect is strongest at $\theta = 0^\circ$ and is not clearly observed at other angles. When the impact angle is $\theta = 30^\circ$, an impactor accretes onto the target and heats the mantle near the impact site. At $\theta = 60^\circ$, the impactor hits the targets twice and the target mantle is more uniformly heated. The target's iron becomes more fragmented during the impact process. At $\theta = 90^\circ$, the impactor grazes the target mantle and does not accrete onto the target at $v_{\text{imp}} \geq 1.1 v_{\text{esc}}$. For $v_{\text{imp}} = v_{\text{esc}}$ cases, see discussion in Section 3.1.3.

3.1.2. Analytical models for ΔKE and ΔPE

As a first step for describing the total internal energy gain ΔIE , we describe the initial kinetic energy of the system KE_0 as

$$KE_0 = \frac{1}{2} \frac{M_t M_i}{M_t + M_i} v_{\text{imp}}^2, \quad (2)$$

where M_t and M_i are the target and impactor masses. Assuming perfect accretion and ignoring any shape change of the post-impact body, the gain of the potential energy due to an impact, ΔPE , is expressed as

$$\Delta PE = -\frac{3}{5} \frac{GM_t^2}{R_t} - \frac{3}{5} \frac{GM_i^2}{R_i} - \frac{GM_t M_i}{R_t + R_i} + \frac{3}{5} \frac{G(M_t + M_i)^2}{R'}, \quad (3)$$

where G is the gravitational constant, R_t and R_i are the radii of the target and impactor bodies, respectively. R' represents the radius of a body whose mass is $M_t + M_i (= M_T)$ (the mass-radius relationship between M_T and R' is described in Section S.1.1). The first and second terms are the gravitational binding energies of the target and impactor bodies. The third term represents the gravitational energy of the impactor body in the gravity potential of the target body, and the fourth term is the gravitational binding energy of the post-impact body under the assumption that the target and impactor perfectly merge. Equation (3) is an idealized potential energy gain assuming a perfect accretion event and the actual potential energy release can differ from this because some mass can be lost and because the mass-radius relationship also can change if the internal temperature of the body changes (see Section S.1.2), which is not considered in Equation 3. Nevertheless, ΔPE still gives a first order estimate for the potential energy change during an impact.

3.1.3. Fitting models for ΔIE , the mantle mass, and the fractional heating

We assume that the total internal energy gain is a function of ΔIE and ΔKE , and is expressed by the Legendre polynomials P_l as

$$\Delta IE(\theta) = (KE_0 + \Delta PE) \sum_{l=0}^{n_e} e_l P_l(\cos \theta), \quad (4)$$

where P_l denotes Legendre polynomial l and e_l is the corresponding coefficients (see Tables S.5-S.6) and n_e is the order of the polynomial. The scaled kinetic energy $\Delta IE/(KE_0 + \Delta PE)$ can exceed 1 because our estimate of ΔPE is an idealized model and the actual ΔPE value can differ, as discussed in Section 3.1.2. In Figure 4a, b, our best fit model is shown as a thick black line, which is

modeled by sixth order Legendre polynomials ($n_e = 6$). The left and right panels represent the $v_{\text{imp}} = v_{\text{esc}}$ and the $v_{\text{imp}} \geq 1.1v_{\text{esc}}$ cases, respectively. The coefficients e_l are determined by linear regression. The error σ is

$$\sigma = \sqrt{\frac{1}{n} \sum_{i=1}^n \left(\frac{\Delta IE_{\text{SPH},i} - \Delta IE_i}{KE_0 + \Delta PE} \right)^2}, \quad (5)$$

where $\Delta IE_{\text{SPH},i}$ is the internal energy gain from an SPH simulation whose ID is i and ΔIE_i is the internal energy gain estimated with our model for ID= i . n is the total number of simulations we consider ($n = 64$ is for $v_{\text{imp}} = v_{\text{esc}}$ and $n = 44$ for $v_{\text{imp}} \geq 1.1v_{\text{esc}}$). The values of σ are calculated for the rest of the models in a similar manner (Figure 4). minimizing the errors between the model and SPH output and are listed in Tables S.5 and S.6. The colors of the lines represent different γ values (for details, see the figure caption). The scaled internal energy gain $\Delta IE/(KE_0 + \Delta PE)$ at $v_{\text{imp}} = v_{\text{esc}}$ is typically larger than that at $v_{\text{imp}} \geq 1.1v_{\text{esc}}$. This is because impacts at $v_{\text{imp}} = v_{\text{esc}}$ result in nearly perfect mergers, which can efficiently convert the impact kinetic energy and potential energy into internal energy; however, this does not always hold for cases with higher impact velocity cases ($v_{\text{imp}} \geq 1.1v_{\text{esc}}$), which often result in hit-and-run collisions especially at large impact angles ($\theta = 60^\circ, 90^\circ$) (e.g., Asphaug 2009; Genda et al. 2012). This scaled internal energy gain decreases as the impact angle increases for the same reason; at large impact angles, the kinetic and potential energies are not efficiently converted into internal energy.

In Figure 4c, d, the fractional heating of the mantle with respect to the total kinetic energy, $\Delta IE_{\text{mantle}}/\Delta IE$ is shown as a function of the impact angle. The fitting model $h(\theta)$ for this parameter at $v_{\text{imp}} = v_{\text{esc}}$ is expressed as

$$h(\theta) = \sum_{l=0}^{n_g} g_l P_l(\cos \theta), \quad (6)$$

where the coefficients g_l are listed in Table S.5 ($n_g = 2$). At $v_{\text{imp}} \geq 1.1v_{\text{esc}}$, we still use the same formula with different coefficients (g'_l in Table S.6). $h(\theta)$ generally increases at larger impact angles for the following reasons; an impact at a small impact angle is energetic enough to heat the core in addition to the mantle, whereas an impact at a larger impact angle tends to heat only the mantle and it is not energetic enough to heat the core. This effect can also be seen in Figure 3, where the core is shock heated at $\theta = 0^\circ$, whereas almost no strong heating occurs at $\theta = 90^\circ$.

The mass of a post-impact body resulting from a low

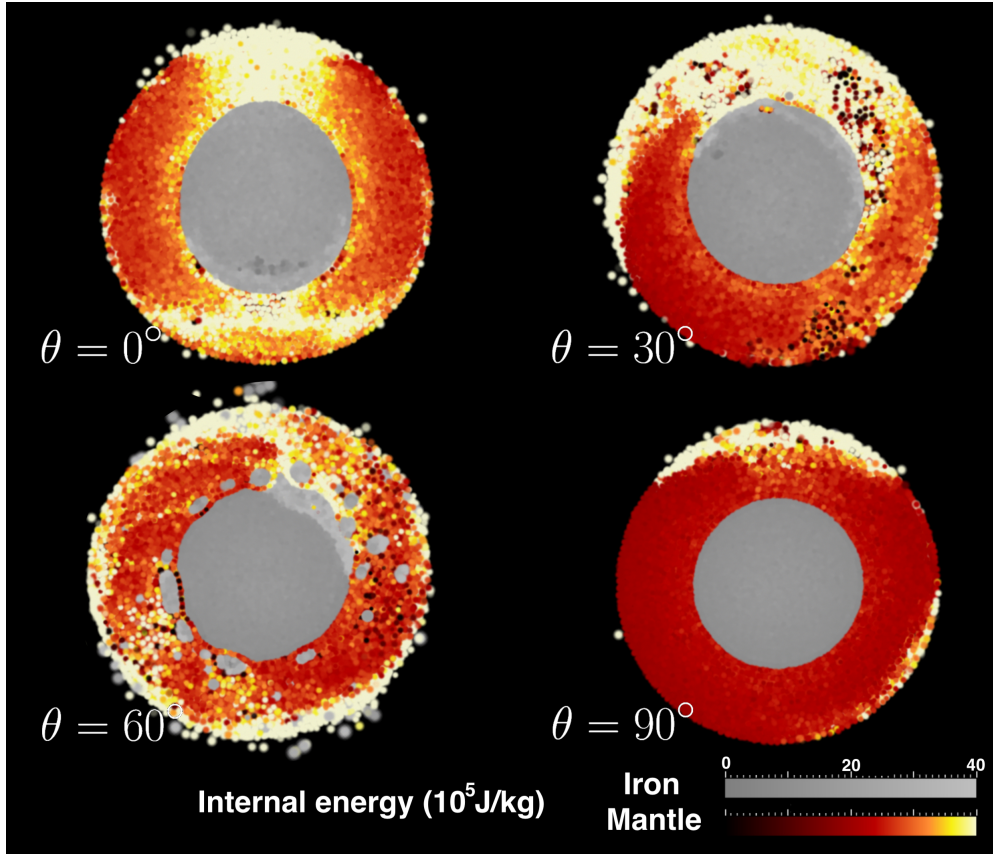


Figure 3: Examples of SPH simulations (Model series M0 - see Table 2. $M_T = 1M_{\text{Mars}}$, $\gamma = 0.1$, $v_{\text{imp}} = v_{\text{esc}}$). The four panels show the results for different impact angles. The grey and red-orange colors represent the internal energy of the iron core and silicate mantle, respectively (the values are shown in 10^5 J/kg). $\psi = 0^\circ$ is placed in the direction of 12 o'clock. The internal energy gain strongly depends on the impact angle.

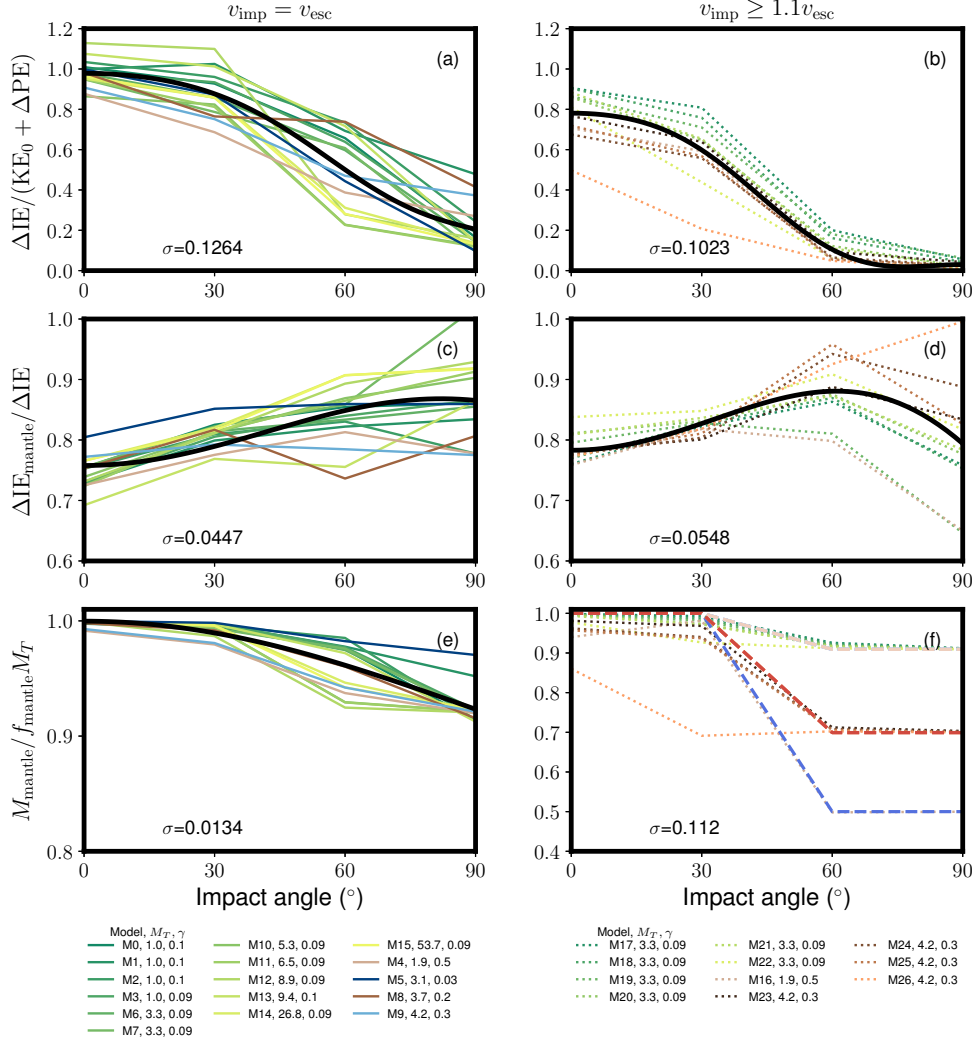


Figure 4: Empirical fits for various parameters. (a, b) The total internal energy gain normalized by the initial kinetic energy KE_0 and ΔPE . The solid and dotted lines represent $v_{\text{imp}} = v_{\text{esc}}$ and $v_{\text{imp}} \geq 1.1v_{\text{esc}}$ cases, respectively. The colors of the lines represent γ values; green-yellow lines (M0-M3, M6-M7, M10-M15, M17-M22) for $\gamma = 0.09 - 0.1$, light brown (M4, M16) for $\gamma = 0.5$, blue (M5) for 0.03, brown (M8) for 0.2, skyblue (M9, M23-M26) for $\gamma = 0.3$. (c, d) The fractional heating of the mantle with respect to the total heating. (e) $M_{\text{mantle}}/f_{\text{mantle}}M_T$ represent the extent of perfect or imperfect accretion at $v_{\text{imp}} = v_{\text{esc}}$. (f) Same as (e) but at $v_{\text{imp}} \geq 1.1v_{\text{esc}}$. The label names correspond to the models listed in Tables S.1-S.3 and the black lines indicate fitted lines (expect in panel f). The standard deviation σ is listed in each panel (Equation 5).

velocity impact is modeled as (Figure 4e)

$$M_{\text{mantle}}(\theta) = f_{\text{mantle}}(M_t + M_i) \sum_{l=0}^{n_k} k_l P_l(\cos \theta), \quad (7)$$

where $n_k = 1$ and the coefficients k_l are listed in Table S.5. The best fit is shown in Figure 4c and the corresponding coefficients k_l are listed in Table S.5 ($n_k = 1$). At $\theta = 0^\circ$, a target and impactor perfectly accrete, but up to $\approx 10\%$ of the total mass is lost at $\theta = 90^\circ$. At $v_{\text{imp}} \geq 1.1v_{\text{esc}}$, the mantle mass of a post-impact body is not well captured by Equation 7, which assumes almost perfect accretion, because high velocity impacts tend to result in hit-and-run collisions. At larger impact velocities, we use the following simple imperfect accretion model (shown in dashed lines in Figure 4f),

$$M_{\text{mantle}}(\theta) = \begin{cases} f_{\text{mantle}}(M_t + M_i), & \text{at } 0^\circ \leq \theta \leq 30^\circ \\ f_{\text{mantle}}[M_t - M_i(\frac{\theta}{30} - 2)], & \text{at } 30^\circ < \theta \leq 60^\circ \\ f_{\text{mantle}}M_t, & \text{at } 60^\circ < \theta \leq 90^\circ. \end{cases} \quad (8)$$

It should be noted that at $v_{\text{imp}} = v_{\text{esc}}$ and $\theta = 90^\circ$, ΔIE estimated from an SPH simulation is underestimated in some cases. An impactor hits the surface of the target and continues to orbit around the target and eventually hits the target again. However, some of the SPH simulations are stopped before an impactor comes back because we only run simulations up until ≈ 25 hours, where the effect of numerical viscosity becomes not negligible (Canup, 2004). This can be seen in Figure 4e, where some impactors accrete into targets while others do not.

3.1.4. Bulk heating model

Figure 5 a ($v_{\text{imp}} = 1.1v_{\text{esc}}$) and b ($v_{\text{imp}} \geq 1.1v_{\text{esc}}$) show estimates of the mass fractions of mantle melt based on our simple model

$$f_{\text{melt}} = \frac{h(\theta)\Delta IE(\theta)}{M_{\text{mantle}}(\theta)E_M}, \quad (9)$$

where E_M is the specific energy necessary to reach the liquidus temperature when the materials cool adiabatically (Bjorkman and Holsapple, 1987). The underlying assumption here is that the initial mantle temperature is at the solidus and the impact-induced heat is used to heat the mantle. Criteria of this type have been widely used in previous studies (e.g., Abramov et al. 2012; Pierazzo and Melosh 2000).

Figure 5c-f shows the melt mass fractions based on the SPH simulations based on various criteria: (Figure 5c,d) entropy gain exceeds 500 J/K/kg (Nakajima

and Stevenson, 2015) (calculated melt mass fractions are listed as MF in Tables S.1-S.3), (Figure 5e, f) temperature exceeds the bridgmanite melting temperature ($T[\text{K}] = 2500 \text{ K} + 26P [\text{GPa}] - 0.052P^2 [\text{GPa}^2]$ where P is the pressure, Solomatov and Stevenson, 1993) (listed as MF_A in Tables S.1-S.3), and (Figure 5g, h) internal energy gain exceeds the latent heat (defined as $7.18 \times 10^5 \text{ J/kg}$, Navrotsky 1995) (listed as MF_L in Tables S.1-S.3). More recent models of the melting temperature exist (e.g., Stixrude and Karki 2005; Stixrude et al. 2009) but we are using this formulation for simplicity.

The entropy criterion is motivated by first principle calculations that suggest that the entropy of melting depends only weakly on the pressure (Stixrude and Karki, 2005; Stixrude et al., 2009). The last criterion ignores the work done by compression, and therefore would overestimate melting if the internal energy criterion at low pressure is used. For Earth-sized planets, compression would increase the internal energy by $-PdV = P/\rho^2 d\rho \sim 6 \times 10^5 \text{ J/kg}$ if $\rho \approx 4000 \text{ kg/m}^3$, $d\rho \approx 1000 \text{ kg/m}^3$, and $P \approx 10 \text{ GPa}$. Here V is the specific volume, and ρ is the density. To offset this effect, the criterion value is set to be relatively high ($7.18 \times 10^5 \text{ J/kg}$).

At $v_{\text{imp}} = v_{\text{esc}}$, the general trend is captured by our model. Interestingly, the melt criteria results shown in Figure 5 c, e, and g are fairly different, but the trends of the melt mass fractions are similar. As a result, even though the melt criterion for Figure 5g, h (a single value of latent heat of melting for the entire mantle) is simple, it may still act as an acceptable melt model. At $v_{\text{imp}} \geq 1.1v_{\text{esc}}$, the melt model does not work as well as the model at $v_{\text{imp}} = v_{\text{esc}}$, partly because our model underestimates heating at $\gamma = 0.1$ (Figure 4b).

The model here assumes that heat is uniformly distributed in the mantle, but this is not the case as shown by our SPH simulations (Figure 3). Thus, in Section 3.2, we will consider the distribution of heat within a mantle.

3.2. Heat distribution model

The heat distribution within a planetary mantle is also modeled with Legendre polynomials. We define the spatial heat distribution function $F(r', \psi, \phi)$ as

$$F(r', \psi, \phi) = F(r', \psi) \equiv \frac{\Delta U(r', \psi)}{\Delta \bar{U}} \approx \frac{\Delta U(r', \psi)}{\Delta IE}, \quad (10)$$

where r' is the normalized radius (0 at the center and 1 at the planetary surface), ψ is the colatitude, and ϕ is the azimuth (see Figure 2b). We assume that the heat distribution is symmetric along the pole and therefore the

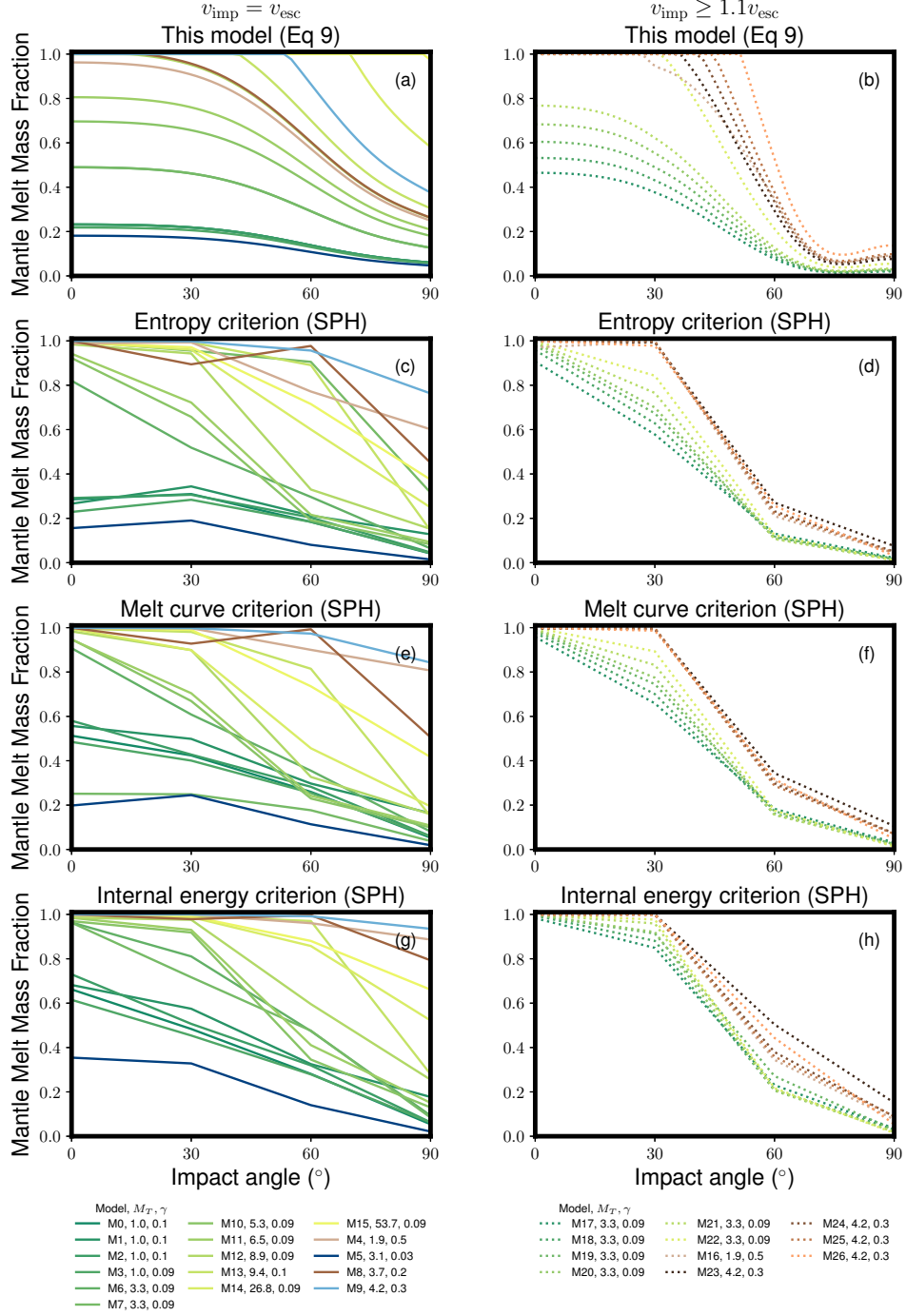


Figure 5: Melt mass fraction at $v_{\text{imp}} = v_{\text{esc}}$ (left panel) and $v_{\text{imp}} \geq 1.1v_{\text{esc}}$ (right panel). The panels (a) and (b) use the melt model defined by Equation 9, the panels (c) and (d) use the estimate based on the entropy criterion, the panels (e) and (f) use the melt curve from Solomatov and Stevenson (1993), and the panels (g) and (h) use a constant internal energy criterion. The model details are discussed in Section 3.1.

model does not depend on ϕ . ψ is defined as zero where the impact-induced heating is maximum, which often coincides with the impact point. $\Delta U(r', \psi)$ is the specific internal energy gain at r' and ψ . $\Delta \bar{U}$ is the average specific internal energy gain. We assume $\Delta \bar{U} \approx \Delta IE$. Here, $F(r', \psi) = F_{r'}(r')F_\psi(\psi)$ is assumed, where

$$F_{r'}(r') = F_{r'}(r'^{-2}, r'^{-1}, 1, r'^1, r'^2), \quad (11)$$

$$F_\psi(\psi) = F_\psi(P_0(\cos \psi), P_1(\cos \psi), P_2(\cos \psi)). \quad (12)$$

This leads to

$$F(r', \psi) = \sum_{m=-2}^2 \sum_{l=0}^2 c_{l+3(m+2)} r'^m P_l(\cos \psi). \quad (13)$$

These expressions require $5 \times 3 = 15$ coefficients c in Equation 13, which are determined as follows. We divide an SPH simulation output into 8×12 segments as a function of radius and angle, $r'_i - \frac{1}{2}\Delta r' < r' < r'_i + \frac{1}{2}\Delta r'$ and $\psi_j - \frac{1}{2}\Delta \psi < \psi < \psi_j + \frac{1}{2}\Delta \psi$ ($\Delta r' \approx 0.5/8 = 0.0625$ and $\Delta \psi = \pi/6$). For this, we only consider SPH particles that satisfy at $|z| < 0.2R'$, where z is the vertical distance from the impact plane at $z = 0$. To define the location of $\psi = 0$, we calculate the averaged internal energy gain at each ψ segment ($\psi_j - \frac{1}{2}\Delta \psi < \psi < \psi_j + \frac{1}{2}\Delta \psi$ and $0.55 < r' < 1$), and we identify the value of ψ at which this value is maximum. The 15 coefficients in Equation 13 are determined by minimizing the error between the model and the averaged internal energies in all the segments (see Table S.7). It should be noted that the coefficients are determined using all the SPH simulations, including both low and high impact velocity cases. We also explored higher orders ($r'^{-3}, r'^3, P_3(\cos \psi)$), but their effects were limited and therefore we remove these terms from the model.

The results for $F(r', \psi)$ are shown in Figure 6. The antipodal heating is well captured at $\theta = 0^\circ$, which is not seen in the case of the other impact angles. Interestingly, the mantle is heated more uniformly at small impact angles ($\theta = 0^\circ, 30^\circ$) than at larger impact angles ($\theta = 60^\circ, 90^\circ$). This finding may seem counter-intuitive, but this can be explained given that an impact with a small impact angle often results in accretion, which is an efficient way to heat the whole mantle, whereas an impact with a large angles heats only the near surface regions of the target body.

3.3. Comparison between our heat model and SPH

Based on Equation 10, the internal energy gain due to an impact is modeled as

$$\Delta U(r', \psi, \theta) = F(r', \psi)\Delta IE(\theta). \quad (14)$$

Figures 7 and 8 show the internal energy gain model ΔU (right) and SPH simulations (left) for the models M0 and M17, respectively. Here, the internal energy gain is normalized by 10^5 J/kg. L_2 is described as

$$L_2 = \sqrt{\sum_{i=1}^{n_{r'}} \sum_{j=1}^{n_\psi} \left(\frac{\Delta IE_{\text{SPH}}(r'_i, \psi_j)}{\Delta IE(r'_i, \psi_j)} - 1 \right)^2}, \quad (15)$$

where $n_{r'} = 8$ and $n_\psi = 12$. The L_2 values are normalized by 10^5 J/kg. In general, the overall trend is captured in our model; at $\theta = 0^\circ$, the mantle is extensively heated near the impact site and antipodal site, whereas the mantle remains colder at $\psi = 90^\circ$ and -90° . At $\theta = 30^\circ$, the mantle on the hemisphere close to the impact ($|\psi| < 90^\circ$) is significantly heated, whereas the other side of the hemisphere ($90^\circ < |\psi| < 180^\circ$) is much less shock-heated. At $\theta = 60^\circ$ for M0, a portion of the mantle near the core mantle boundary is highly shock heated. This is because part of the mantle is locally heated while the impactor's core sinks to the bottom. At $\theta = 90^\circ$, our model underestimates impact-induced heating in models M0 and M17 primarily because our ΔIE model also underestimates heating (Figure 4 a,b).

3.4. Effect of the initial temperature

In this section, we explore the geometry of a magma ocean by considering an initial thermal profile of the mantle. In Figure 9, the top panels (a) and (b) represent the internal energy gain and melt fraction, respectively. Here, part of the mantle is considered to be molten when the internal energy gain is larger than the latent heat L . The underlying assumption for this melt criterion is that the mantle temperature is on solidus before the impact. This may be appropriate for large protoplanets with a steam atmosphere because of their long cooling timescales (Solomatov and Stevenson, 1993; Abe, 1997; Nakajima and Stevenson, 2015) compared to the timescales between impacts. However, depending on the water content and size of the planet, this assumption may not be valid. If the protoplanet is small, or if the protoplanet has a silicate atmosphere, it can cool quickly until crystalization progresses enough such that cooling is controlled by solid state convection (e.g., Elkins-Tanton, 2012).

Figure 9c shows the total internal energy (i.e. internal energy gain + initial internal energy) with $S_0 = 3160$ J/K/kg, where S_0 is the entropy of an adiabatic mantle. This corresponds to the surface temperature of ≈ 2000 K. Here we assume that the initial thermal profile of a mantle does not affect the internal energy gain. Figure 9e also shows the total internal energy with $S_0 = 1100$

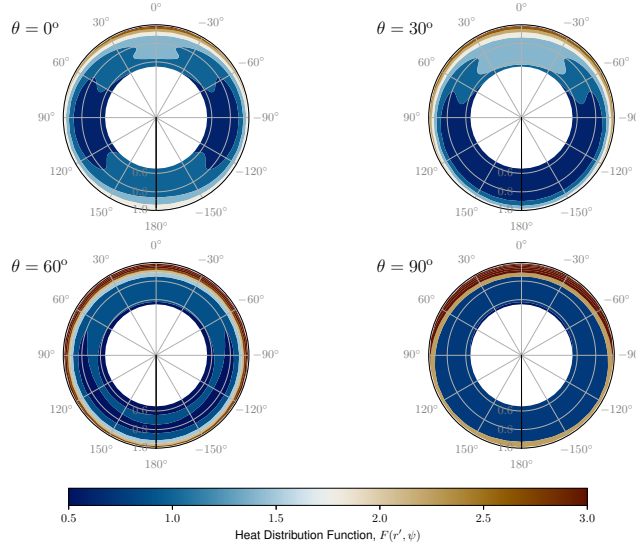


Figure 6: Normalized heat distribution model $F(r', \psi)$ (Equation 13) for different impact angles ranging from 0 to 90°. The internal energy is normalized by the averaged energy of the system.

J/K/kg, which corresponds to a surface temperature of ≈ 300 K. Such adiabatic profiles are calculated using M-ANEOS. Part of the mantle is considered to be molten if its temperature exceeds the melt temperature (Section 3.1.4). For simplicity we use for the internal energy $u = c_v T$, where c_v is the specific heat and T is the temperature. As seen in the figure, the melt mass fraction depends on the initial thermal profile. For the case with the “cold” initial thermal profile (panels e and f), a fraction of the internal energy gain is used to heat the mantle up to solidus, resulting in much smaller melt mass fraction compared to the “warm” scenario (panels c and d).

3.5. Magma ocean depth and the corresponding pressure

Our model describes the geometry of a magma ocean as follows. In this section, we use a simple model in which part of the mantle is considered to be molten if its internal energy gain exceeds L (i.e. the initial temperature is assumed to be on the solidus). Here, D' is the normalized depth of a magma ocean or a melt pool; a deep magma ocean is represented by a large value of D' (the maximum D' is ≈ 0.55 , which is as deep as the core-mantle boundary). We define three D' s; $D'_{\text{Melt pool}}$, the depth of a melt pool (Figure 1b); $D'_{\text{Global MO}}$ the depth of a global magma ocean (Figure 1a and Figure 10c) assuming that the magma volume is the same as that of the melt pool model, and $D'_{\text{Bulk heating}}$, the depth of a radially

uniform magma ocean whose melt volume is estimated from Equation (9). For the melt pool and the global magma ocean cases, the melt volumes are the same. For the melt pool case, we define the depth of the magma ocean as the largest D' at $\psi = 0^\circ$. $D'_{\text{Melt pool}}$ is always larger than $D'_{\text{Global MO}}$. Differences between $D'_{\text{Melt pool}}$ and $D'_{\text{Bulk heating}}$ depend on the choice of E_M and L .

Figure 10 shows magma ocean depths (left panels) and equivalent pressures at the bottom of the magma oceans (right panels) for $v_{\text{imp}} = v_{\text{esc}}$ cases. This pressure is calculated assuming the post-impact body is in a hydrostatic equilibrium (no spin is considered) and the density-pressure profile is the same as the profile of an adiabatic mantle with $S_0 = 3160$ J/K/kg. The magma ocean depth can significantly depend on the model if the impact does not entirely melt the mantle. For example, in Model M7, the pressures are 39, 22, and 10 GPa for the melt pool, global magma ocean, and bulk heating models, respectively, at $\theta = 60^\circ$. The difference tends to increase at large impact angles and can reach 10-50 % under certain circumstances. These pressure differences can affect estimating element partitioning, as discussed in Section 4.3.

4. Discussion

4.1. Python script on the melt scaling laws on GitHub

We provide a Python script for this model on GitHub. In this script, $\Delta IE(\theta)$ is computed based on the fitting

Model: M0

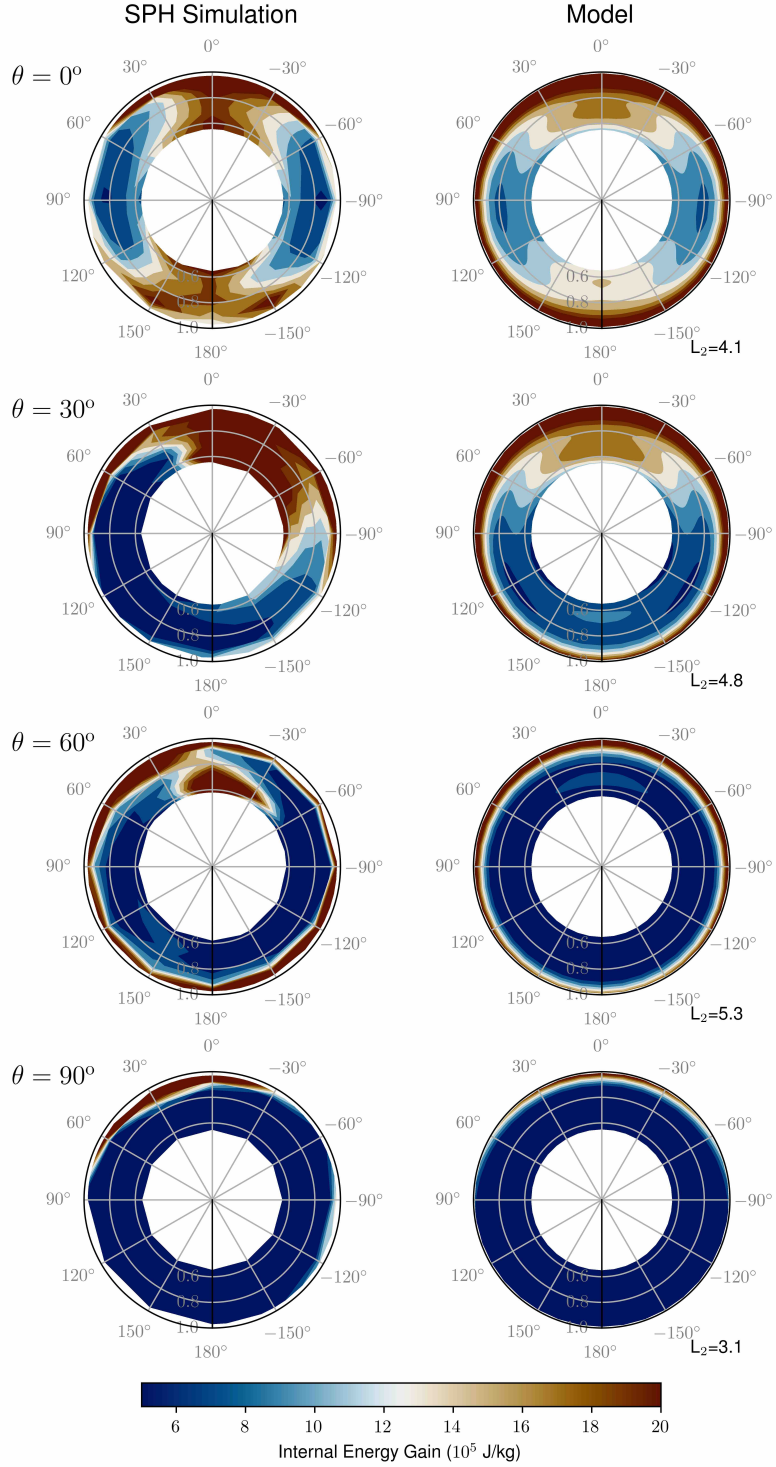


Figure 7: Comparison between SPH results (left) for M0 model series (Table S.1) and the scaling law (right) for (top row) $\theta = 0^\circ$, (second row) 30° , (third row) 60° , (bottom row) 90° , respectively. The input parameters are $M_T = 1M_{\text{Mars}}$, $\gamma = 0.1$, $v_{\text{imp}} = v_{\text{esc}}$. The color contour represents the internal energy normalized to 10^5 J/kg after the system reaches its equilibrium (typically within 10 hours).

Model: M17

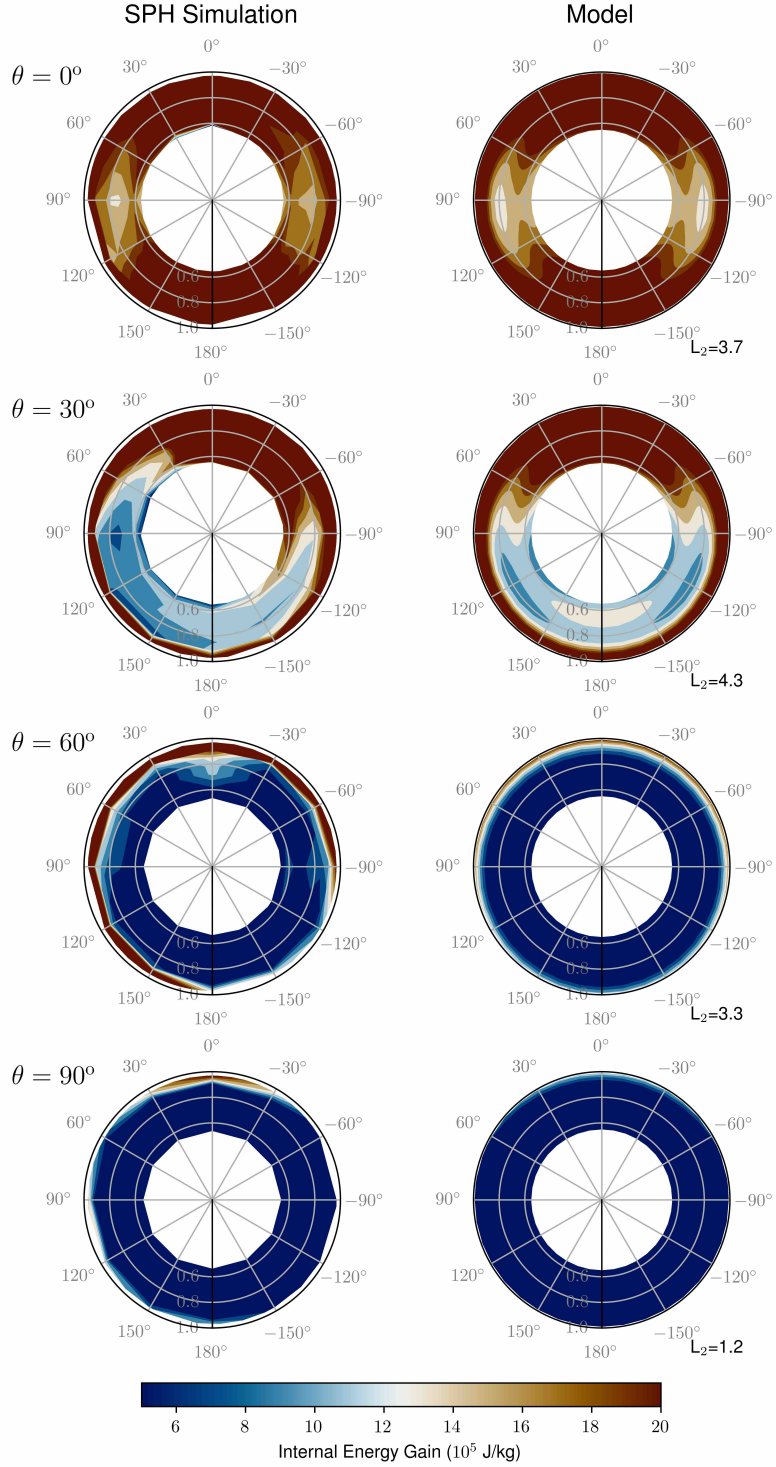


Figure 8: SPH results for M17 (Table S.3). The color scheme is the same as the one in Figure 7. The input parameters are $M_T = 3.25M_{\text{Mars}}$, $\gamma = 0.091$, $v_{\text{imp}} = 1.2v_{\text{esc}}$.

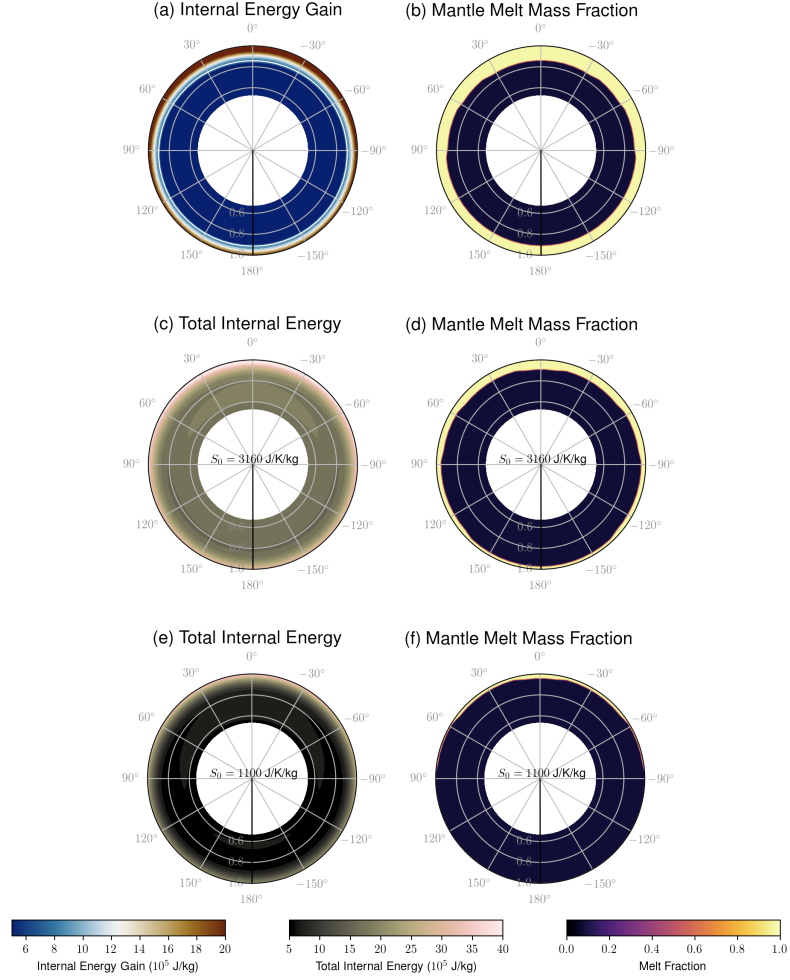


Figure 9: Effect of initial temperature is considered for Model M0 at $\theta = 60^\circ$. (a) Internal energy gain as calculated in Equation 14. The white line represents where the internal energy gain is the same as the latent heat L , and 0 when it is smaller than L . (b) Melt mass fraction, where this value is 1 when the internal energy gain is larger than L , and 0 when it is smaller than L . (c) Total internal energy (internal energy gain + initial internal energy) where the entropy value $S_0 = 3160$ J/K/kg (the initial surface temperature is ≈ 2000 K). (d) Melt mass fraction using the model (c). The melt criterion from Solomatov and Stevenson (1993) is used. (e) Same as (c), but with the initial entropy $S_0 = 1100$ J/K/kg, which corresponds to ≈ 300 K at the surface. (f) Same as (d) but for $S_0 = 1100$ case. For details, see the main text.

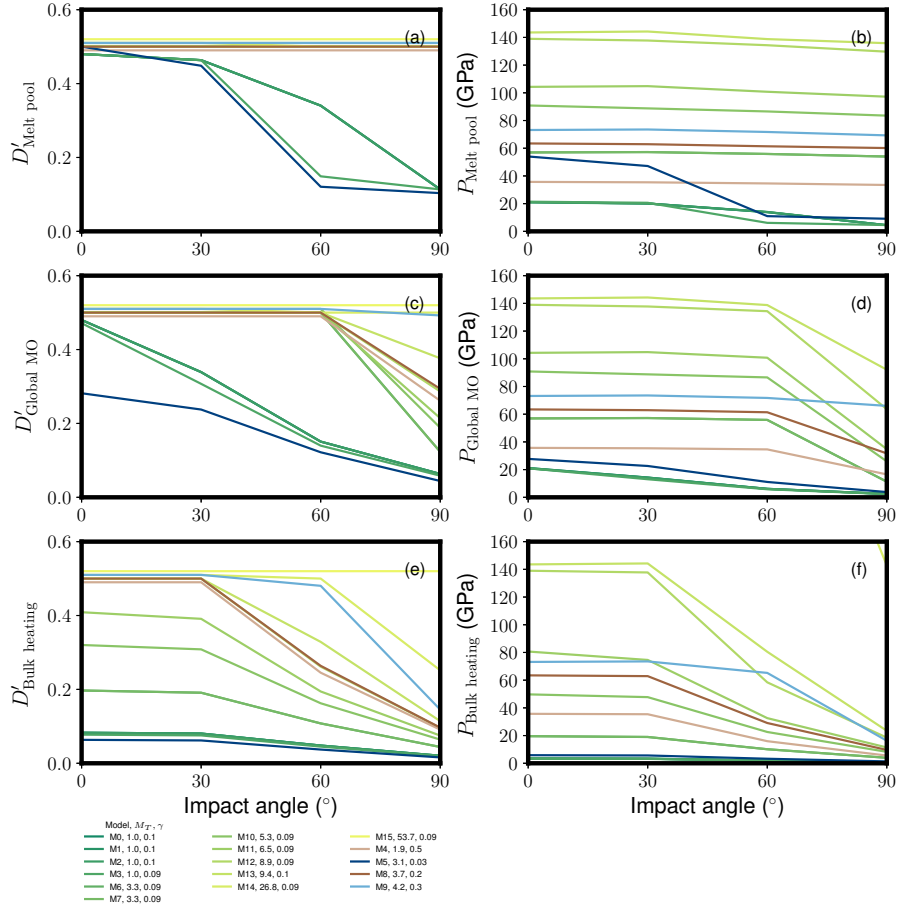


Figure 10: The depth of the magma ocean and corresponding pressure at $v_{\text{imp}} = v_{\text{esc}}$. (a) The normalized radius of the melt pool from the analytical model using the spatial distribution $F(r', \psi)$ (Equation 13) at $v_{\text{imp}} = v_{\text{esc}}$ (Figure 1b). Panel (c) represents an isostatically readjusted, radially uniform magma ocean (Figure 1a). Panel (e) represents a radially uniform magma ocean whose volume is estimated by the bulk heating model represented by Equation 9. The panels (b, d, f) display the corresponding pressures at the base of the melt pool or magma ocean.

model we develop (Equation 4) as a function of the impact angle θ , total mass M_T , impactor-to-total mass ratio γ , and impact velocity v_{imp} . Impact-induced heating is modeled using Equation 13. The initial thermal state of the mantle can be selected from the following options; (a) on solidus, (b) $S_0 = 1100$ J/K/kg, and (c) $S_0 = 3160$ J/K/kg, but we are planning to add more options. So far we calculate the size and depth of a magma ocean as well as the corresponding pressure using the criterion from Solomatov and Stevenson (1993), but this can be modified easily.

Our simulations do not include cases at $v_{\text{esc}} < v_{\text{imp}} < 1.1v_{\text{esc}}$. In our Python script, we linearly interpolate e_l between values $v_{\text{imp}} = v_{\text{esc}}$ and $v_{\text{imp}} \geq 1.1v_{\text{esc}}$. Additional information, such as $h(\theta)$ and $M_{\text{mantle}}(\theta)$, is not needed to calculate magma ocean shapes and depths, but is included for the sake of completeness in the script. In Section 3.1.2, we consider $v_{\text{imp}} = v_{\text{esc}}$ and $v_{\text{imp}} \geq 1.1v_{\text{esc}}$ separately, and assume that an impactor and target do not merge at $\theta = 60^\circ, 90^\circ$. However, this is a simplified assumption and it needs to be modified. In the script, we use v_{cr} as derived in Genda et al. (2012),

$$\frac{v_{\text{cr}}}{v_{\text{esc}}} = c_1 \Gamma^2 \Theta^{c_5} + c_2 \Gamma + c_3 \Theta^{c_5} + c_4, \quad (16)$$

where $\Gamma = (M_t - M_i)/M_T$ and $\Theta = 1 - \sin \theta$, $c_1 = 2.43$, $c_2 = -0.0408$, $c_3 = 1.86$, $c_4 = 1.08$, $c_5 = 5/2$. When $v_{\text{imp}} < v_{\text{cr}}$, the low velocity criteria ($v_{\text{imp}} = v_{\text{esc}}$) are used, whereas when $v_{\text{imp}} > v_{\text{cr}}$, the high velocity criteria ($v_{\text{imp}} \geq 1.1v_{\text{esc}}$) are used.

4.2. Model simplifications

Our SPH simulations take into account the latent heat of silicate vaporization, but the effect is not explicitly considered in our analytical melt model. For more energetic impacts than considered here, vaporization is likely to play a more important role. However, in such a scenario it is likely that the majority of the post-impact mantle experiences melting, and therefore a detailed melt scaling law may not be necessary when vaporization matters (see Section S.1.2 for detailed discussion).

We assume that the initial thermal profile of a planet does not affect the internal energy gain. This is probably a fine assumption given that the density change due to temperature is relatively small (for example, 1000 K difference makes $\Delta\rho \sim \rho\alpha\Delta T \sim 3000 \text{ kg m}^{-3} \times 10^{-5} \text{ K}^{-1} \times 1000 \text{ K} = 30 \text{ kg m}^{-3}$). We also ignore the heating dependence on the azimuth (ϕ) for simplicity. This should be fine for $\theta = 0^\circ$ cases, but this is not the case for other impact angles. Thus, heating dependence on the colatitude needs to be investigated in future studies.

4.3. Implications for elemental partitioning

Whether an isostatic readjustment takes place or not during metal-silicate equilibration determines whether the melt pool model or the global magma ocean model is relevant. The timescale for isostatic readjustment depends on the magma ocean length scale and the viscosity of the solid target body mantle (Reese and Solomatov, 2006). The isostatic readjustment timescale can be estimated roughly as $4\pi\eta/(\rho g\lambda)$ (Turcotte and Schubert, 2014), where η is the dynamic viscosity of a solid target body mantle, ρ is the mantle density, g is the gravity, and λ is the length scale of the magma ocean. Assuming a relatively warm solid mantle (and therefore a low viscosity value, 10^{18} Pa s) with a 1000 km length scale, this time scale is ≈ 10 years, which is much longer than the equilibration times scale (within hours - months, e.g., Landeau et al. 2016). Of course, this timescale depends on the choice of parameters, especially the mantle solid viscosity, but a spatially confined, melt pool is likely a more relevant geometry for metal-silicate equilibration (e.g., Fig 3, Rubie et al., 2015).

As seen in Figures 10, the pressure at the base of the magma ocean can vary considerably based on different magma ocean models. This would affect partitioning of elements because the metal-silicate partitioning depends on the equilibration pressures and temperatures, which are often associated with the values at the base of the magma ocean (e.g., Rubie et al., 2015). If a melt pool is a more appropriate geometry than a global magma ocean, we may need to revise our models on the elemental abundances in planetary cores and mantles. For example, more light elements, such as Mg, Si, and O, may be present in the Earth's core, which are considered to be partitioned into the core under high pressure and temperature conditions (e.g., Siebert et al. 2013; Fischer et al. 2015; O'Rourke and Stevenson 2016), which could affect heat flux, magnetic field, and seismic observations even today (e.g., Labrosse 2015).

This paper only considers the initial condition of a magma ocean, but it is important to consider its time evolution to calculate element equilibration processes. de Vries et al. (2016) point out that a small impactor, which does not generate a magma ocean, can still contribute to the metal-silicate equilibration process if it falls into a pre-existing magma ocean. Moreover, in this scenario, the magma ocean depth decreases over time due to crystallization, making the effective magma ocean depth smaller than the initial value.

4.4. Material strength and choice of EOS

We do not consider the effect of material strength in this work, which can be important under certain

conditions (e.g., Quintana et al., 2015; Golabek et al., 2018; Emsenhuber et al., 2018; Kurosawa and Genda, 2018). Material strength is known to matter for relatively small impacts (Benz and Asphaug, 1999), where plastic causes additional melting (Kurosawa and Genda, 2018). In contrast, the effect is likely limited for large and high velocity impacts because shock heating becomes more important than heating due to plastic deformation at high velocity impacts, which is also consistent with work based on impact simulations (Quintana et al., 2015). If an impact is energetic and the peak pressure exceeds the elastic limit (0.1 – 10 GPa, Jeanloz e.g., 1980), treating the material as a fluid is probably appropriate. Genda et al. (2017) also argue that material strength does not play a significant role when the target radius is larger than 100 km. Emsenhuber et al. (2018) investigate a large impact between a Mars-sized target and a 1000 km-sized impactor assuming that these bodies are either entirely solid with material strength or fluid without strength. They find that heating is more prominent in solid than in fluid, but the actual extent of heating may lie in between because the mantle should experience melting and transition from solid to fluid. Thus, the effect of material strength needs further studies, but it is likely limited for large impacts.

The choice of EOS also affects the outcome. The Tillotson EOS is not be an appropriate choice because it does not adequately describe the thermodynamics of the system. The choice of input parameters for M-ANEOS can be important because it affects the extent of shock heating and vaporization (Stewart et al., 2019). We will further investigate its effect in our future study.

4.5. Relationship between E_M and L

The specific energy necessary to reach the liquidus temperature at 1 atm, E_M , has been widely used in previous studies to estimate impact-induced melt volumes (e.g., Pierazzo et al., 1997; Abramov et al., 2012; de Vries et al., 2016). A wide range of values of E_M is used and is not often physically well motivated (E_M is usually much larger than the latent heat L). There are several challenges to use E_M for estimating melt volumes. First, the value of E_M should depend on the initial depth of the materials inside of the target, but this dependence is usually ignored. Secondly, such bulk heating models (as discussed in Section 3.1.4) ignore the distribution of heat within the target and assume that the impact uniformly heats the target. They make it challenging to determine the appropriate value of E_M .

4.6. Resolution

Figure S.2 shows a resolution test for the SPH simulations. We find that the melt mass fraction is not sensitive to the SPH resolution shown in the range of values of $N = 10^4$ to 10^5 , where N is the number of SPH particles. We further investigate whether the resolution affects the heating distribution within the mantle. Simulations shown in Figures S.3 ($N = 10^4$ and $N = 5 \times 10^4$) use the same input parameters as those in Figure 7 ($N = 10^5$) but with fewer SPH particles. The $N = 5 \times 10^4$ case is very similar to the $N = 10^5$ case, but the $N = 10^4$ case does not capture the details very well. Based on these results, we mostly use a few 10^4 to 10^5 particles for this study.

5. Conclusions

We develop mantle melt scaling laws as a function of the impact angle, impact velocity, total mass, and impactor-to-total mass ratio based on more than 100 SPH simulations. Our scaling laws include an analytical expression for the spatial heat distribution as a function of Legendre polynomials. Our scaling laws reproduce the heat distribution within a mantle computed by SPH simulations relatively well. We also find that the pressure difference at the base of a global (radially homogeneous) magma ocean, often used in literature, and a spatially confined melt pool can reach 10-50 %. This pressure difference could affect the pressure calculations for the metal-silicate equilibration in a magma ocean and subsequently affects the estimations for core and mantle chemistry of forming protoplanets and could affect the long-term evolution of the core. The scaling laws are publicly available via GitHub.

Acknowledgements

We thank our two anonymous reviewers for helpful comments that significantly improved this manuscript. We also thank Alessandro Morbidelli, Francis Nimmo, and Stéphane Labrosse for helpful discussions. We acknowledge support from the Carnegie DTM fellowship as well as the European Research Council (ERC) Advanced Grant ACCRETE (Contract No. 290568) and the German Science Foundation (DFG) Priority Programme SPP1833 Building a Habitable Earth (RU 1323/10-1). K.W. and L.M. are funded by Deutsche Forschungsgemeinschaft (DFG) grant SFB-TRR 170 (C4), TRR-170 Pub. No. 75. The calculations were partly carried out on the GRAPE system. The perceptually-uniform color maps used in Figures 6-9 was provided by Fabio Cramer (Cramer, 2018).

References

- Abe, Y., 1997. Thermal and chemical evolution of the terrestrial magma ocean. *Physics of the Earth and Planetary Interiors* 100, 27–39.
- Abramov, O., Wong, S.M., Kring, D.A., 2012. Differential melt scaling for oblique impacts on terrestrial planets. *Icarus* 218, 906–916.
- Agnor, C., Asphaug, E., 2004. Accretion efficiency during planetary collisions. *Astrophys. J.* 613, 157–160.
- Agnor, C.B., Canup, R.M., Levison, H.F., 1999. On the character and consequences of large impacts in the late stage of terrestrial planet formation. *Icarus* 142, 219–237.
- Asphaug, E., 2009. Growth and evolution of asteroids. *Annual Review of Earth and Planetary Sciences* 37, 413–48.
- Barr, A.C., Citron, R.I., 2011. Scaling of melt production in hypervelocity impacts from high-resolution numerical simulations. *Icarus* 211, 913–916.
- Benz, W., Anic, A., Horner, J., Whitby, J.A., 2007. The Origin of Mercury. *Space Science Reviews* 132, 189–202.
- Benz, W., Asphaug, E., 1999. Catastrophic disruptions revisited. *Icarus* 142, 5–20.
- Bjorkman, M.D., Holsapple, K.A., 1987. Velocity scaling impact melt volume. *Int. J. Impact Eng.* 5, 155–163.
- Cameron, A.G.W., Ward, W.R., 1976. The origin of the moon. *Lunar Planet. Sci. VII*, 120.
- Canup, R.M., 2004. Simulations of a late lunar-forming impact. *Icarus* 168, 433–456.
- Canup, R.M., 2005. A giant impact origin of Pluto-Charon. *Science* 307, 546–50.
- Canup, R.M., Salmon, J., 2018. Origin of Phobos and Deimos by the impact of a Vesta-to-Ceres sized body with Mars. *Science Advances* 4, eaar6887.
- Citron, R.I., Genda, H., Ida, S., 2015. Formation of Phobos and Deimos via a giant impact. *Icarus* 252, 334–338.
- Craddock, R.A., 2011. Are Phobos and Deimos the result of a giant impact? *Icarus* 211.
- Crameri, F., 2018. Geodynamic diagnostics, scientific visualisation and staglab 3.0. *Geoscientific Model Development* 11, 2541–2562.
- Dahl, T.W., Stevenson, D.J., 2010. Turbulent mixing of metal and silicate during planet accretion - and interpretation of the Hf-W chronometer. *Earth Planet. Sci. Lett.* 295, 177–186.
- Deguen, R., Landeau, M., Olson, P., 2014. Turbulent metal-silicate mixing, fragmentation, and equilibration in magma oceans. *Earth and Planetary Science Letters* 391, 274–287.
- Elkins-Tanton, L.T., 2012. Magma oceans in the inner solar system. *Annual Review of Earth and Planetary Sciences* 40, 113–139.
- Emsenhuber, A., Jutzi, M., Benz, W., 2018. SPH calculations of Mars-scale collisions: The role of the equation of state, material rheologies, and numerical effects. *Icarus* 301, 247–257.
- Fischer, R.A., Nakajima, Y., Campbell, A.J., Frost, D.J., Harries, D., Langenhorst, F., Miyajima, N., Pollok, K., Rubie, D.C., 2015. High pressure metal-silicate partitioning of Ni, Co, V, Cr, Si, and O. *Geochimica et Cosmochimica Acta* 167, 177–194.
- Genda, H., Fujita, T., Kobayashi, H., Tanaka, H., Suetsugu, R., Abe, Y., 2017. Impact erosion model for gravity-dominated planetesimals. *Icarus* 294, 234–246.
- Genda, H., Kokubo, E., Ida, S., 2012. Merging criteria for giant impacts of protoplanets. *The Astrophysical Journal* 744, 137.
- Golabek, G.J., Emsenhuber, A., Jutzi, M., Asphaug, E.I., Gerya, T.V., 2018. Coupling sph and thermochemical models of planets: Methodology and example of a mars-sized body. *Icarus* 301, 235–246.
- Hartmann, W.K., Davis, D.R., 1975. Satellite-sized planetesimals and lunar origin. *Icarus* 24, 504–514.
- Hyodo, R., Genda, H., Charnoz, S., Pignatale, F.C., Rosenblatt, P., 2018. On the impact origin of phobos and deimos iv: Volatile depletion. *The Astronomical Journal* 860, 150.
- Jeanloz, R., 1980. Shock effects in olivine and implications for hugoniot data. *Journal of Geophysical Research* 85, 3163–3176.
- Kegerreis, J.A., Teodoro, L.F.A., Eke, V.R., Massey, R.J., Catling, D.C., Fryer, C.L., Korycansky, D.G., Warren, M.S., Zahnle, K.J., 2018. Consequences of Giant Impacts on Early Uranus for Rotation, Internal Structure, Debris, and Atmospheric Erosion. *The Astrophysical Journal* 861, 52.
- Kurosawa, K., Genda, H., 2018. Effects of Friction and Plastic Deformation in Shock-Comminuted Damaged Rocks on Impact Heating. *Geophysical Research Letters* 45, 620–626.
- Labrosse, S., 2015. Thermal evolution of the core with a high thermal conductivity. *Physics of the Earth and Planetary Interiors* 247, 36–55.
- Landeau, M., Olson, P., Deguen, R., Hirsh, B.H., 2016. Core merging and stratification following giant impact. *Nature Geoscience* 9, 786–789.
- Leinhardt, Z.M., Stewart, S.T., 2012. Collisions between gravity-dominated bodies. i. outcome regimes and scaling laws. *The Astrophysical Journal* 745, 79.
- Lherm, V., Deguen, R., 2018. Small-scale metal/silicate equilibration during core formation: The influence of stretching enhanced diffusion on mixing. *Journal of Geophysical Research: Solid Earth* 123, 10,496–10,516.
- Lock, S.J., Stewart, S.T., 2017. The structure of terrestrial bodies: Impact heating, corotation limits, and synestias. *Journal of Geophysical Research: Planets* 122, 950–982.
- McKinnon, W.B., 1988. On the origin of triton and pluto. *Nature* 311, 355–358.
- McKinnon, W.B., 1989. On the origin of the pluto-charon binary. *Astrophysical Journal* 344, L41–44.
- Melosh, H.J., 2007. A hydrocode equation of state for SiO₂. *Meteorit. Planet. Sci.* 42, 2079–2098.
- Monaghan, J.J., 1992. Smoothed particle hydrodynamics. *Annu. Rev. Astron. Astrophys.* 30, 543–574.
- Monteux, J., Arkani-Hamed, J., 2019. Shock wave propagation in layered planetary interiors: Revisited. *Icarus* 331, 238–256.
- Nakajima, M., Canup, R.M., 2017. Origin of the martian moons and their water abundances. *Lunar and Planetary Science Conference*, 2900.
- Nakajima, M., Stevenson, D.J., 2014. Investigation of the initial state of the moon-forming disk: Bridging sph simulations and hydrostatic models. *Icarus* 233, 259–267.
- Nakajima, M., Stevenson, D.J., 2015. Melting and mixing states of the earth's mantle after the moon-forming impact. *Earth and Planetary Science Letters* 427, 286–295.
- Navrotsky, A., 1995. Thermodynamic properties of minerals. In: Ahrens TJ (ed) *Mineral physics and crystallography*. American Geophysical Union, Washington, DC, USA, 18–28.
- O'Rourke, J.G., Stevenson, D.J., 2016. Powering earth's dynamo with magnesium precipitation from the core. *Nature* 529, 387–389.
- Pierazzo, E., Melosh, H.J., 2000. Melt production in oblique impacts. *Icarus* 145, 252–261.
- Pierazzo, E., Vickery, A.M., Melosh, H.J., 1997. A reevaluation of impact melt production. *Icarus* 127, 408–423.
- Quintana, S.N., Crawford, D.A., Schultz, P.H., 2015. Analysis of Impact Melt and Vapor Production in CTH for Planetary Applications. *Procedia Engineering* 103, 499–506.
- Reese, C., Solomatov, V., 2006. Fluid dynamics of local martian magma oceans. *Icarus* 184, 102–120.
- Rosenblatt, P., 2011. The origin of the martian moons revisited. *The Astronomy and Astrophysics Review* 19, 44.
- Rosenblatt, P., Charnoz, S., Dunseath, K.M., Terao-Dunseath, M., Trinh, A., Hyodo, R., Genda, H., Toupin, S., 2016. Accretion of

Phobos and Deimos in an extended debris disc stirred by transient moons. *Nature Geoscience* 9, 581–583.

Rubie, D. C., Melosh, H.J., Reid, J.E., Liebske, C., Righter, K., 2003. Mechanisms of metal-silicate equilibration in the terrestrial magma ocean. *Earth and Planetary Science Letters* 205, 239–255.

Rubie, D.C., Frost, D.J., Mann, U., Asahara, Y., Nimmo, F., Tsuno, K., Kegler, P., Holzheid, A., Palme, H., 2011. Heterogeneous accretion, composition and core-mantle differentiation of the earth. *Earth and Planetary Science Letters* 301, 31–42.

Rubie, D.C., Jacobson, S.A., Morbidelli, A., O’Brien, D.P., Young, E.D., de Vries, J., Nimmo, F., Palme, H., Frost, D.J., 2015. Accretion and differentiation of the terrestrial planets with implications for the compositions of early-formed solar system bodies and accretion of water. *Icarus* 248, 89–108.

Safronov, V.S., 1969. In evolution of the protoplanetary cloud and formation of the earth and planets. Israel Program for Scientific Translations.

Shoemaker, E.M., 1962. Interpretation of lunar craters. Z. Kopal (Ed.), *Physics and Astronomy of the Moon*, Academic, New York, 283–359.

Siebert, J., Badro, J., Antonangeli, D., Ryerson, F.J., 2013. Terrestrial accretion under oxidizing conditions. *Science* 339, 1194–1197.

Slattery, W.L., Benz, W., Cameron, A.G.W., 1992. Giant impact on a primitive uranus. *Icarus* 99, 167–174.

Solomatov, V.S., Stevenson, D.J., 1993. Nonfractional crystallization of a terrestrial magma ocean. *Journal of Geophysical Research* 98, 5391–5406.

Stevenson, D.J., 1990. Fluid dynamics of core formation. Newton, H. E. and Jones, J.H. (Ed.), *Origin of the Earth*. Oxford University Press, New York, 231–250.

Stewart, S.T., Davies, E.J., Duncan, M.S., Lock, S.J., Root, S., Townsend, J.P., Kraus, R.G., Caracas, R., Jacobsen, S.B., 2019. The shock physics of giant impacts: Key requirements for the equations of state, arXiv:1910.04687.

Stewart, S.T., Leinhardt, Z., 2012. Collisions between gravity-dominated bodies. ii. the diversity of impact outcomes during the end stage of planet formation. *The Astronomical Journal* 751, 32.

Stixrude, L., Karki, B., 2005. Structure and Freezing of MgSiO_3 Liquid in Earths Lower Mantle. *Science* 310, 297–299.

Stixrude, L., de Koker, N., Sun, N., Mookherjee, M., Karki, B., B., 2009. Thermodynamics of silicate liquids in the deep earth. *Earth and Planetary Science Letters* 278, 226–232.

Thompson, S.L., Lauson, H.S., 1972. Improvements in the CHART D radiationhydrodynamics code III: revised analytic equation of state. Sandia National Laboratories, Albuquerque, New Mexico, 119p.

Tonks, W.B., Melosh, J., 1993. Magma ocean formation due to giant impacts. *J. Geophys. Res.* 98, 5319–5333.

Tonks, W.B., Melosh, J.H., 1992. Core formation by giant impacts. *Icarus* 100, 326–346.

Turcotte, D., Schubert, G., 2014. *Geodynamics*, third edition. Cambridge University Press.

de Vries, J., Nimmo, F., Melosh, H.J., Jacobson, S.A., Morbidelli, A., Rubie, D.C., 2016. Impact-induced melting during accretion of the Earth. *Progress in Earth and Planetary Science* 3, 7.

Wade, J., Wood, B.J., 2005. Core formation and the oxidation state of the Earth. *Earth and Planetary Science Letters* 236, 78–95.

Ward, W.R., 1993. Density waves in the solar nebula. *Icarus* 106, 274–827.

Wünnemann, K., Collins, G.S., Melosh, H.J., 2006. A strain-based porosity model for use in hydrocode simulations of impacts and implications for transient crater growth in porous targets. *Icarus* 180, 514–527.

Supplementary Materials

S.1. Model descriptions

S.1.1. Mass-radius relationship

As discussed in Section 3.1, the planetary radius R' whose mass is $M_T + M_i$ is described as $R' = R_0[(M_t + M_i)/M_0]^{\Gamma(M)}$, where $R_0 = 1.5717 \times 10^6$ m and $M_0 = 6.39 \times 10^{22}$ kg and $\Gamma(M) = \sum_{i=0}^3 b_i [\ln(M/M_0)]^i$. The mass-radius relationship is shown in Figure S.1 and b_i are listed in Table S.4. We compute the radius of a planet by integrating the mass of a thin shell ($4\pi r^2 dr$) from the center of the planet until the mass reaches the targeted planetary mass. We assume that the mantle and core are isentropic (entropy values for the mantle and core are 3160 J/K/kg and 1500 J/K/kg, respectively) and that the planet is in a hydrostatic equilibrium. The density-pressure relationship is computed based on M-ANEOS. We find that using a constant value of the exponent ($\Gamma \approx 0.3$) introduces an error and therefore we decide to use a variable Γ .

Figure S.2 shows calculated melt mass fractions (MA) computed with several resolutions. We find that the melt mass fraction is not sensitive to the SPH resolution shown in this range. Figures S.3-S.4 show internal energy gains in 10^5 J/kg in Models M1 and M2, which use the same input parameters as Model M0 (Figure 7) with different resolutions (10^4 and 5×10^4 , respectively). The details are discussed in Section 4.6.

S.1.2. Additional output parameters

Additional parameters are listed in Tables S.8-S.10. VMF is the vapor mass fraction, T_{spin} is the spin orbital time in hours, I_x and I_z are the moments of inertia along x axis and z axis, respectively, where the z axis is perpendicular to the impact plane (the impact occurs in the $x - y$ plane). Here there is practically no difference between the x and y axes if a post-impact body rotates. At $\theta = 0^\circ$, the impact point is at $x = 0$ and the post-impact body is practically not rotating.

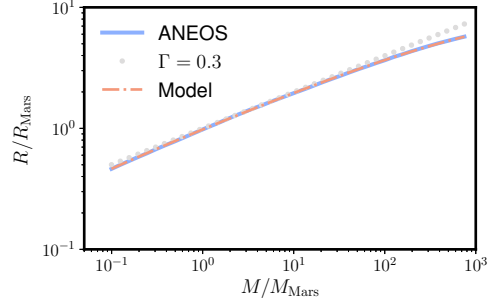


Figure S.1: Mass-radius relationship for planets with an adiabatic mantle and core. The mantle and core fractions are 0.7 and 0.3, respectively.

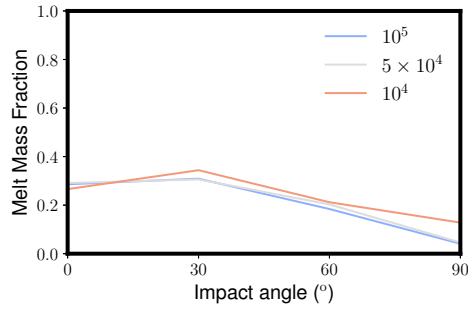


Figure S.2: SPH resolution test of the melt mass fraction (models M0-M2). Blue, grey, and red lines represent results using 10^5 , 5×10^4 , and 10^4 SPH particles, respectively.

Model: M1

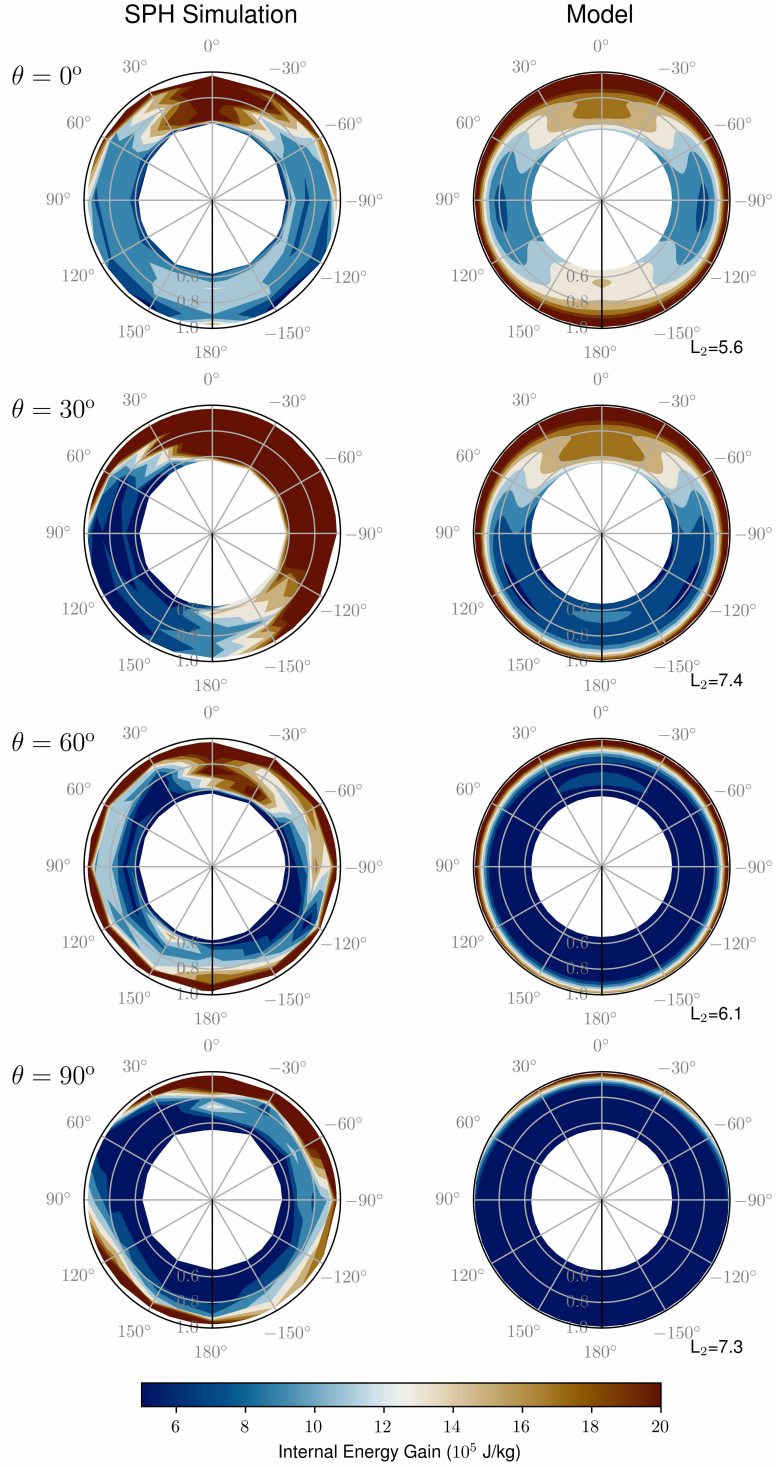


Figure S.3: This figures is the same as Figure 7 ($N = 10^5$), with $N = 10^4$. The overall trend of the heat distribution is similar to the one in Figure 7, but some details, such as antipodal heating at $\theta = 0^\circ$ are not well captured.

Model: M2

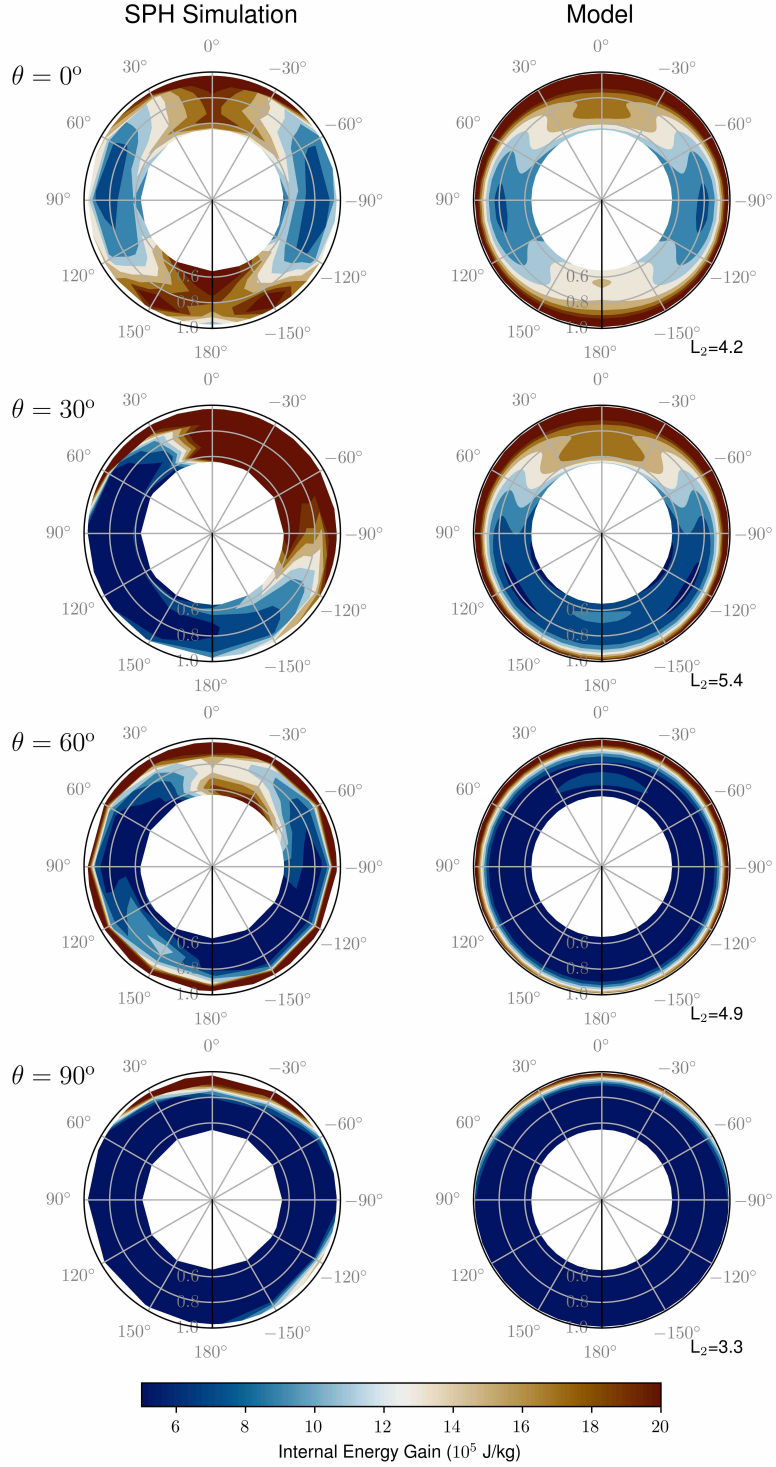


Figure S.4: This figures is the same as Figures 7 ($N = 10^5$) and S.3, with $N = 5 \times 10^4$. The is more similar to Figure 7; antipodal heating at $\theta = 0^\circ$ is well captured.

Run	ID	M_T	γ	θ	$v_{\text{imp}}/v_{\text{esc}}$	v_{esc}	dE	$\frac{dE_{\text{mantle}}}{dE}$	$\frac{M_{\text{mantle}}}{M_T}$	MF	MF_A	MF_L	L_2	N
M0	1	1.0	0.1	0	1.0	4246	7.054e+29	0.754	0.998	0.286	0.513	0.662	4.104	100000
M0	2	1.0	0.1	30	1.0	4246	6.478e+29	0.825	0.994	0.309	0.424	0.484	4.755	100000
M0	3	1.0	0.1	60	1.0	4246	4.59e+29	0.855	0.975	0.184	0.26	0.281	5.265	100000
M0	4	1.0	0.1	90	1.0	4246	1.149e+29	0.861	0.914	0.041	0.053	0.054	3.134	100000
M1	5	1.0	0.1	0	1.0	4246	6.983e+29	0.729	0.998	0.266	0.557	0.682	5.645	10000
M1	6	1.0	0.1	30	1.0	4246	7.162e+29	0.799	0.997	0.344	0.499	0.575	7.389	10000
M1	7	1.0	0.1	60	1.0	4246	4.844e+29	0.822	0.978	0.212	0.297	0.325	6.107	10000
M1	8	1.0	0.1	90	1.0	4246	3.345e+29	0.834	0.952	0.128	0.163	0.177	7.261	10000
M2	9	1.0	0.1	0	1.0	4246	7.229e+29	0.752	0.998	0.291	0.58	0.73	4.159	50000
M2	10	1.0	0.1	30	1.0	4246	6.71e+29	0.809	0.996	0.306	0.428	0.507	5.42	50000
M2	11	1.0	0.1	60	1.0	4246	5.129e+29	0.83	0.985	0.203	0.283	0.32	4.922	50000
M2	12	1.0	0.1	90	1.0	4246	1.7e+29	0.777	0.914	0.046	0.06	0.063	3.304	50000
M3	13	1.03	0.091	0	1.0	4401	6.7e+29	0.731	0.999	0.229	0.485	0.615	5.23	16500
M3	14	1.03	0.091	30	1.0	4401	6.35e+29	0.805	0.997	0.284	0.401	0.454	7.14	16500
M3	15	1.03	0.091	60	1.0	4401	4.342e+29	0.84	0.977	0.184	0.255	0.279	7.071	16500
M3	16	1.03	0.091	90	1.0	4401	1.283e+29	0.866	0.923	0.043	0.059	0.062	4.409	16500
M4	17	1.88	0.5	0	1.0	5061	4.778e+30	0.725	0.992	0.988	0.997	0.998	4.3	30000
M4	18	1.88	0.5	30	1.0	5061	3.739e+30	0.775	0.979	0.994	0.998	1.0	5.091	30000
M4	19	1.88	0.5	60	1.0	5061	2.114e+30	0.813	0.937	0.772	0.9	0.961	3.685	30000
M4	20	1.88	0.5	90	1.0	5061	1.469e+30	0.777	0.92	0.601	0.807	0.887	2.686	30000
M5	21	3.06	0.032	0	1.0	6622	1.671e+30	0.804	1.0	0.156	0.198	0.354	8.585	31000
M5	22	3.06	0.032	30	1.0	6622	1.458e+30	0.852	0.998	0.19	0.245	0.328	8.498	31000
M5	23	3.06	0.032	60	1.0	6622	7.423e+29	0.859	0.982	0.08	0.114	0.14	4.953	31000
M5	24	3.06	0.032	90	1.0	6622	1.635e+29	0.859	0.97	0.014	0.019	0.021	2.784	31000
M6	25	3.25	0.091	0	1.0	6473	4.697e+30	0.726	0.999	0.82	0.907	0.964	3.695	33000
M6	26	3.25	0.091	30	1.0	6473	4.115e+30	0.814	0.996	0.519	0.608	0.811	3.851	33000
M6	27	3.25	0.091	60	1.0	6473	2.874e+30	0.834	0.975	0.296	0.355	0.474	3.116	33000
M6	28	3.25	0.091	90	1.0	6473	6.881e+29	0.855	0.921	0.064	0.081	0.093	1.383	33000
M7	29	3.25	0.091	0	1.0	6527	4.558e+30	0.755	0.999	0.999	0.251	0.963	3.379	33000
M7	30	3.25	0.091	30	1.0	6527	3.782e+30	0.822	0.993	0.956	0.249	0.717	5.317	33000
M7	31	3.25	0.091	60	1.0	6527	2.917e+30	0.858	0.976	0.905	0.177	0.476	2.43	33000
M7	32	3.25	0.091	90	1.0	6527	4.55e+29	1.019	0.92	0.315	0.038	0.084	1.809	33000
M8	33	3.7	0.2	0	1.0	6546	1.114e+31	0.753	0.998	1.0	0.999	1.0	3.423	37500
M8	34	3.7	0.2	30	1.0	6546	8.654e+30	0.817	0.992	0.894	0.928	0.979	3.052	37500
M8	35	3.7	0.2	60	1.0	6546	8.354e+30	0.736	0.96	0.977	0.993	0.996	2.35	37500
M8	36	3.7	0.2	90	1.0	6546	4.688e+30	0.807	0.915	0.45	0.506	0.793	2.842	37500
M9	37	4.23	0.301	0	1.0	6757	1.681e+31	0.772	0.993	1.0	1.0	1.0	3.69	42900
M9	38	4.23	0.301	30	1.0	6757	1.392e+31	0.793	0.981	0.998	0.998	1.0	4.023	42900
M9	39	4.23	0.301	60	1.0	6757	8.701e+30	0.785	0.942	0.956	0.973	0.992	2.988	42900
M9	40	4.23	0.301	90	1.0	6757	6.898e+30	0.775	0.921	0.763	0.843	0.935	2.605	42900

Table S.1: List of parameters at $v_{\text{imp}} = v_{\text{esc}}$. M_T is the total mass normalized by the Martian mass, γ is the impactor-to-total mass ratio, θ is the impact angle (0° is a head-on collision). v_{imp} is the impact velocity, and v_{esc} is the mutual escape velocity in m/s, and dE is the impact-induced energy in J, and dE_{mantle}/dE is the fraction of the energy that goes into the mantle, and M_{mantle} is the final mantle mass of the accreted mantle, f_{mantle} is the mantle mass fraction (0.7), MF , MF_A , and MF_L are the calculated melt mass fraction of the mantle with different melt criteria (see the main text for details). L_2 is the normalized L_2 norm. N is the number of SPH particles.

VMF is calculated as

$$VMF = \frac{1}{n} \sum_i^n \begin{cases} 0, & \text{at } S_i < S_{\text{liquid}}, \\ \frac{S_i - S_{\text{liquid}}}{S_{\text{vapor}} - S_{\text{liquid}}}, & \text{at } S_{\text{liquid}} \leq S_i \leq S_{\text{vapor}}, \\ 1, & \text{at } S_{\text{liquid}} < S_i. \end{cases} \quad (\text{S.1})$$

where i represents an SPH particle, S_i is the entropy of the SPH particle i , n is the number of mantle SPH particles. S_{vapor} and S_{liquid} are the entropies of the vapor and liquid at the phase boundary (these values depend on temperature). The vapor mass fraction of a post-impact body is generally small for most of the simulations, but is large when the total mass is large ($M_T = 26.84M_{\text{Mars}}$ and $54M_{\text{Mars}}$ in M14 and M15) or the impact velocity is large ($M_T = 4.23M_{\text{Mars}}$, $v_{\text{imp}} = 1.6v_{\text{esc}}$ at $\theta = 0^\circ$ in M26). In these scenarios, the mantles experience almost complete melting. Thus, our assumption that vaporization does not affect estimating the mass of a magma ocean seems acceptable (VMF also depends on the choice of EOS).

T_{spin} is calculated based on the angular velocity, which is estimated by dividing the angular momentum along the z axis by I_z . At $\theta = 0^\circ$, a post-impact body is not rotating, which makes T_{spin} large, but not infin-

ity. This is because the boundary between a post-impact body and ejecta is not clearly defined and calculating the exact moment of inertia or L_z is challenging. Nevertheless, T_{spin} is generally much larger at $\theta = 0^\circ$ compared to the other cases.

The parameter I_x/I_z is related to the oblateness of a post-impact body. When this value is close to 1, a post-impact body is close to a sphere, whereas a large deviation from 1 means that a body is more oblate. Most of the bodies have values close to $0.8 - 1$, but there are a few exceptions. For example, the model M9 at $\theta = 90^\circ$ (ID 40), $I_x/I_z = 0.452$. These bodies should have lower pressures than calculated pressures assuming the bodies are hydrostatic. We ignore the rotational effect on the pressure because they are rare in our parameter range and because we prefer to keep the equation simple.

S.1.3. Comparison with previous studies

Comparison of melt mass fractions obtained from our study with those of previous studies is shown in Figure S.5. The top panels represent our bulk heating model (see Section 3.1.4) and the bottom panels represent a model that is similar to previous models (Bjorkman and Holsapple, 1987; Pierazzo and Melosh, 2000; Abramov

Run	ID	M_T	γ	θ	$v_{\text{imp}}/v_{\text{esc}}$	v_{esc}	dE (J)	$\frac{dE_{\text{mantle}}}{dE}$	$\frac{M_{\text{mantle}}}{f_{\text{mantle}} M_T}$	MF	MF _A	MF _L	L2	N
M10	41	5.34	0.091	0	1.0	7698	9.691e+30	0.739	0.999	0.923	0.948	0.97	6.382	33000
M10	42	5.34	0.091	30	1.0	7698	9.23e+30	0.812	0.995	0.657	0.669	0.919	3.641	33000
M10	43	5.34	0.091	60	1.0	7698	2.545e+30	0.869	0.929	0.192	0.23	0.346	2.784	33000
M10	44	5.34	0.091	90	1.0	7698	1.395e+30	0.903	0.921	0.083	0.099	0.13	1.396	33000
M11	45	6.54	0.091	0	1.0	8271	1.506e+31	0.724	0.999	0.942	0.946	0.985	4.742	33000
M11	46	6.54	0.091	30	1.0	8271	1.287e+31	0.814	0.995	0.722	0.704	0.93	3.136	33000
M11	47	6.54	0.091	60	1.0	8271	3.599e+30	0.865	0.929	0.216	0.242	0.411	3.086	33000
M11	48	6.54	0.091	90	1.0	8271	1.897e+30	0.913	0.921	0.093	0.108	0.151	0.8993	33000
M12	49	8.94	0.091	0	1.0	9241	3.068e+31	0.731	0.999	0.984	0.983	0.985	6.601	33000
M12	50	8.94	0.091	30	1.0	9241	2.993e+31	0.811	0.987	0.943	0.899	0.976	5.128	33000
M12	51	8.94	0.091	60	1.0	9241	7.589e+30	0.893	0.925	0.33	0.327	0.596	2.576	33000
M12	52	8.94	0.091	90	1.0	9241	4.332e+30	0.929	0.921	0.152	0.159	0.255	1.068	33000
M13	53	9.43	0.104	0	1.0	9217	3.599e+31	0.692	1.0	0.997	0.997	0.995	4.66	33482
M13	54	9.43	0.104	30	1.0	9217	3.392e+31	0.769	0.997	0.993	0.981	0.993	4.293	33482
M13	55	9.43	0.104	60	1.0	9217	2.402e+31	0.755	0.972	0.891	0.815	0.97	1.955	33482
M13	56	9.43	0.104	90	1.0	9217	4.758e+30	0.865	0.913	0.145	0.15	0.28	1.038	33482
M14	57	26.84	0.091	0	1.0	13600	1.73e+32	0.766	1.0	0.995	0.994	0.997	4.04	11000
M14	58	26.84	0.091	30	1.0	13600	1.56e+32	0.82	0.996	0.96	0.899	0.988	3.282	11000
M14	59	26.84	0.091	60	1.0	13600	5.664e+31	0.907	0.946	0.601	0.456	0.858	2.246	11000
M14	60	26.84	0.091	90	1.0	13600	2.472e+31	0.919	0.923	0.249	0.194	0.522	1.038	11000
M15	61	53.66	0.091	0	1.0	17520	5.865e+32	0.766	1.0	0.992	1.0	0.997	4.228	11000
M15	62	53.66	0.091	30	1.0	17520	5.206e+32	0.816	0.996	0.971	0.99	0.991	3.356	11000
M15	63	53.66	0.091	60	1.0	17520	1.709e+32	0.907	0.942	0.715	0.735	0.88	2.12	11000
M15	64	53.66	0.091	90	1.0	17520	7.895e+31	0.917	0.922	0.374	0.417	0.661	0.9534	11000

Table S.2: Continuation of Table S.1.

et al., 2012) based on the relationship,

$$f_{\text{melt}} = k \left(\frac{v_{\text{imp}}^2}{L'} \right)^{3\mu/2} \frac{M_i}{f_{\text{mantle}}(M_t + M_i)} \cos^{1.3} \theta, \quad (\text{S.2})$$

where $k = 0.42$ and $\mu = 0.56$. The overall trend is the same, meaning that the melt mass fractions are larger at small impact angles and with large total and impactor masses. One noticeable difference, however, is that melt mass fraction is non-zero at $\theta = 90^\circ$ in our model, whereas the value is zero in the previous model. As shown in Figures 3 and 4, impact-induced heating is not zero at this impact angle, primarily due to tidal deformation of the target. This effect is not considered in the previous model. In our simulations, tidal deformation and tidal heating are taken into account and these effects are incorporated in our model. At $v_{\text{imp}} \geq 1.1v_{\text{esc}}$, the melt mass fraction hits the lowest point between $\psi = 60-90^\circ$ in some models (for example in M26). This is due to an artifact of model fitting and is not physically motivated. Nonetheless, this effect is relatively minor and does not affect the model in a significant way.

Some of the previous work (e.g., Leinhardt and Stewart, 2012; Lock and Stewart, 2017) develop and use a specific impact energy (this is referred as Q in the studies mentioned above) to describe the total kinetic energy involved in an impact and thus to take into account the dependence of an impact angle on the heating. This is a useful alternative parameter, but it does not take into account tidal deformation and therefore underestimates heating when the impact angle is $\theta = 90^\circ$.

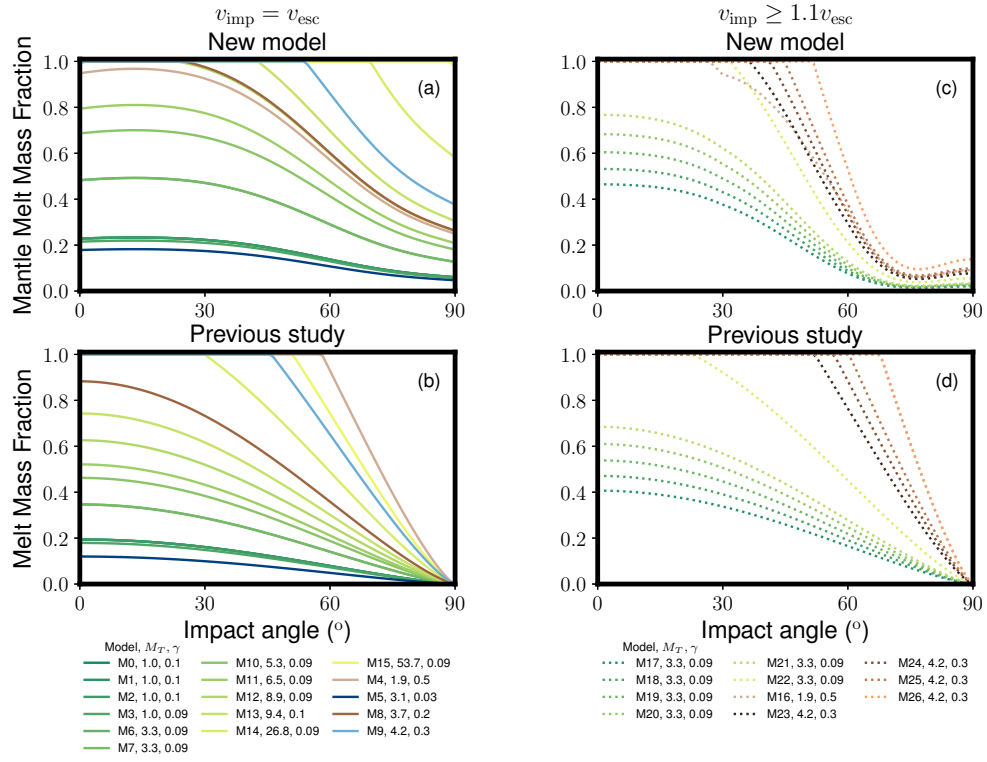


Figure S.5: Comparison with previous studies (See Section S.1.3) at (left) $v_{\text{imp}} = v_{\text{esc}}$ and (right) $v_{\text{imp}} \geq 1.1 v_{\text{esc}}$. The top panels represent our study and the bottom panels represent the previous analytical model.

Run	ID	M_T	γ	θ	$v_{\text{imp}}/v_{\text{esc}}$	v_{esc}	dE (J)	dE_{mantle}/dE	M_{mantle}/M_T	MF	MF _A	MF _L	L2	N
M16	65	1.88	0.5	0	1.3	5061	5.624e+30	0.75	0.937	0.963	0.992	0.997	5.067	30000
M16	66	1.88	0.5	30	1.3	5061	4.744e+30	0.818	0.982	0.995	0.997	1.0	9.992	30000
M16	67	1.88	0.5	60	1.3	5061	4.551e+29	0.798	0.498	0.21	0.308	0.344	2.454	30000
M16	68	1.88	0.5	90	1.3	5061	1.855e+29	0.65	0.5	0.044	0.072	0.076	0.6725	30000
M17	69	3.25	0.091	0	1.1	6473	5.012e+30	0.76	0.999	0.906	0.958	0.983	3.652	33000
M17	70	3.25	0.091	30	1.1	6473	4.47e+30	0.823	0.993	0.578	0.659	0.849	4.287	33000
M17	71	3.25	0.091	60	1.1	6473	1.113e+30	0.863	0.926	0.131	0.183	0.231	3.294	33000
M17	72	3.25	0.091	90	1.1	6473	3.067e+29	0.758	0.912	0.022	0.031	0.035	1.201	33000
M18	73	3.25	0.091	0	1.2	6473	5.724e+30	0.77	0.997	0.958	0.977	0.994	3.128	33000
M18	74	3.25	0.091	30	1.2	6473	4.802e+30	0.826	0.987	0.629	0.7	0.881	3.58	33000
M18	75	3.25	0.091	60	1.2	6473	1.023e+30	0.87	0.922	0.115	0.161	0.208	2.419	33000
M18	76	3.25	0.091	90	1.2	6473	2.657e+29	0.753	0.911	0.018	0.027	0.03	0.7971	33000
M19	77	3.25	0.091	0	1.3	6473	6.224e+30	0.796	0.996	0.98	0.986	0.997	5.109	33000
M19	78	3.25	0.091	30	1.3	6473	5.108e+30	0.828	0.982	0.673	0.745	0.914	3.211	33000
M19	79	3.25	0.091	60	1.3	6473	1.298e+30	0.81	0.919	0.118	0.173	0.271	2.045	33000
M19	80	3.25	0.091	90	1.3	6473	4.493e+29	0.646	0.911	0.015	0.024	0.028	0.7303	33000
M20	81	3.25	0.091	0	1.4	6473	6.987e+30	0.811	0.996	0.992	0.992	0.999	4.508	33000
M20	82	3.25	0.091	30	1.4	6473	5.274e+30	0.831	0.974	0.699	0.774	0.92	2.39	33000
M20	83	3.25	0.091	60	1.4	6473	9.941e+29	0.876	0.917	0.109	0.156	0.206	1.462	33000
M20	84	3.25	0.091	90	1.4	6473	1.672e+29	0.777	0.91	0.012	0.02	0.021	0.4575	33000
M21	85	3.25	0.091	0	1.5	6473	8.071e+30	0.809	0.993	0.995	0.993	1.0	2.512	33000
M21	86	3.25	0.091	30	1.5	6473	5.972e+30	0.836	0.972	0.765	0.831	0.959	2.799	33000
M21	87	3.25	0.091	60	1.5	6473	1.006e+30	0.873	0.916	0.107	0.158	0.211	1.045	33000
M21	88	3.25	0.091	90	1.5	6473	1.548e+29	0.784	0.91	0.011	0.018	0.019	0.4915	33000
M22	89	3.25	0.091	0	2.0	6473	1.232e+31	0.838	0.977	1.0	1.0	1.0	5.133	33000
M22	90	3.25	0.091	30	2.0	6473	6.664e+30	0.848	0.927	0.843	0.893	0.977	3.027	33000
M22	91	3.25	0.091	60	2.0	6473	9.251e+29	0.909	0.912	0.124	0.175	0.217	1.15	33000
M22	92	3.25	0.091	90	2.0	6473	1.138e+29	0.817	0.909	0.009	0.013	0.014	0.5082	33000
M23	93	4.23	0.301	0	1.1	6757	1.623e+31	0.783	0.981	0.998	0.998	0.999	7.463	42900
M23	94	4.23	0.301	30	1.1	6757	1.353e+31	0.801	0.968	0.993	0.993	1.0	2.359	42900
M23	95	4.23	0.301	60	1.1	6757	1.958e+30	0.888	0.712	0.271	0.344	0.504	1.038	42900
M23	96	4.23	0.301	90	1.1	6757	8.952e+29	0.834	0.703	0.075	0.106	0.151	0.603	42900
M24	97	4.23	0.301	0	1.2	6757	1.62e+31	0.775	0.962	0.997	0.996	1.0	9.637	42900
M24	98	4.23	0.301	30	1.2	6757	1.341e+31	0.804	0.94	0.996	0.995	0.999	3.445	42900
M24	99	4.23	0.301	60	1.2	6757	1.556e+30	0.942	0.708	0.232	0.297	0.38	1.312	42900
M24	100	4.23	0.301	90	1.2	6757	5.99e+29	0.888	0.701	0.05	0.072	0.088	1.302	42900
M25	101	4.23	0.301	0	1.3	6757	1.949e+31	0.776	0.957	0.999	0.999	1.0	3.477	42900
M25	102	4.23	0.301	30	1.3	6757	1.543e+31	0.811	0.937	0.999	0.998	1.0	2.972	42900
M25	103	4.23	0.301	60	1.3	6757	1.48e+30	0.958	0.706	0.224	0.287	0.359	2.184	42900
M25	104	4.23	0.301	90	1.3	6757	6.645e+29	0.826	0.701	0.046	0.07	0.09	0.5211	42900
M26	105	4.23	0.301	0	1.6	6757	1.886e+31	0.772	0.86	0.999	0.999	1.0	3.893	42900
M26	106	4.23	0.301	30	1.6	6757	7.866e+30	0.818	0.691	0.978	0.986	0.999	4.588	42900
M26	107	4.23	0.301	60	1.6	6757	1.843e+30	0.925	0.702	0.256	0.316	0.443	1.729	42900
M26	108	4.23	0.301	90	1.6	6757	3.892e+29	0.996	0.7	0.031	0.048	0.054	0.6779	42900

Table S.3: The list of parameters is the same as those in Table S.1, but at $v_{\text{imp}} \geq 1.1v_{\text{esc}}$.

b_0	b_1	b_2	b_3
0.3412	-8.90×10^{-3}	9.1442×10^{-4}	-7.4332×10^{-5}

Table S.4: List of parameters to describe the planetary mass-radius relationship.

e_0	e_1	e_2	e_3	e_4	e_5	e_6
0.18432	0.06338	0.00353	0.06389	0.10604	-0.18243	0.0279
g_0	g_1	g_2	k_0	k_1		
0.81590257	0.04083351	-0.09894310	0.92329251	0.07644334		

Table S.5: List of parameters for the internal energy gain (e_l , Equation 4), for the heat partitioning into the mantle (g_l , Equation 6), and for the mantle mass for a post-impact body (k_l , Equation 7) at $v_{\text{imp}} = v_{\text{esc}}$.

e_0	e_1	e_2	e_3	e_4	e_5	e_6
0.01934962	0.045056792	0.11079199	0.17159203	0.14955157	-0.11510527	-0.015958111
g_0	g_1	g_2				
0.6712941	0.3572683	-0.2455803				

Table S.6: Parameters are the same as Table S.5 at $v_{\text{imp}} \geq 1.1v_{\text{esc}}$.

$\theta = 0^\circ$							
c_0	c_1	c_2	c_3	c_4	c_5	c_6	c_7
29.274	13.520	-11.649	-182.579	-83.471	64.442	422.348	189.340
c_8	c_9	c_{10}	c_{11}	c_{12}	c_{13}	c_{14}	
-132.776	-427.249	-187.415	121.140	160.476	68.592	-40.758	
$\theta = 30^\circ$							
c_0	c_1	c_2	c_3	c_4	c_5	c_6	c_7
34.762	-9.325	-19.128	-220.517	46.203	107.129	516.584	-83.478
c_8	c_9	c_{10}	c_{11}	c_{12}	c_{13}	c_{14}	
-224.151	-527.982	65.573	208.573	199.789	-18.336	-72.599	
$\theta = 60^\circ$							
c_0	c_1	c_2	c_3	c_4	c_5	c_6	c_7
86.224	7.523	-13.151	-533.420	-55.168	76.810	1220.543	144.144
c_8	c_9	c_{10}	c_{11}	c_{12}	c_{13}	c_{14}	
-167.596	-1223.634	-160.886	161.857	454.693	65.585	-58.112	
$\theta = 90^\circ$							
c_0	c_1	c_2	c_3	c_4	c_5	c_6	c_7
132.401	123.638	54.712	-805.472	-745.938	-334.647	1812.815	1669.950
c_8	c_9	c_{10}	c_{11}	c_{12}	c_{13}	c_{14}	
759.928	-1789.317	-1645.015	-759.779	654.879	602.363	282.695	

Table S.7: Model coefficients for $\theta = 0, 30, 60$, and 90° (Equation 13).

Run	ID	M_T	γ	θ	$v_{\text{imp}}/v_{\text{esc}}$	VMF	T_{spin} (hrs)	I_x/I_z	$I_z \times 10^{-37}$
M0	1	1.0	0.1	0	1.0	0.003	1074.830	1.074	0.240
M0	2	1.0	0.1	30	1.0	0.002	8.213	1.006	0.248
M0	3	1.0	0.1	60	1.0	0.005	11.487	0.581	0.396
M0	4	1.0	0.1	90	1.0	0.000	37.781	0.992	0.210
M1	5	1.0	0.1	0	1.0	0.000	316.479	0.997	0.250
M1	6	1.0	0.1	30	1.0	0.001	7.731	0.957	0.255
M1	7	1.0	0.1	60	1.0	0.001	7.007	0.958	0.259
M1	8	1.0	0.1	90	1.0	0.001	11.082	0.980	0.229
M2	9	1.0	0.1	0	1.0	0.002	1717.294	1.034	0.245
M2	10	1.0	0.1	30	1.0	0.002	8.130	0.957	0.252
M2	11	1.0	0.1	60	1.0	0.003	17.015	0.958	0.737
M2	12	1.0	0.1	90	1.0	0.001	34.145	0.996	0.210
M3	13	1.03	0.091	0	1.0	0.000	34470.193	0.968	0.265
M3	14	1.03	0.091	30	1.0	0.001	8.834	0.965	0.265
M3	15	1.03	0.091	60	1.0	0.002	7.635	0.935	0.259
M3	16	1.03	0.091	90	1.0	0.001	41.022	0.792	0.283
M4	17	1.88	0.5	0	1.0	0.046	7530.717	0.784	0.808
M4	18	1.88	0.5	30	1.0	0.013	3.889	0.791	0.919
M4	19	1.88	0.5	60	1.0	0.006	3.641	0.524	1.153
M4	20	1.88	0.5	90	1.0	0.002	6.878	0.827	2.253
M5	21	3.06	0.032	0	1.0	0.006	7991.603	0.938	1.497
M5	22	3.06	0.032	30	1.0	0.005	23.626	0.984	1.502
M5	23	3.06	0.032	60	1.0	0.003	27.831	0.994	1.413
M5	24	3.06	0.032	90	1.0	0.001	149.991	0.998	1.389
M6	25	3.25	0.091	0	1.0	0.006	3396.710	1.003	1.650
M6	26	3.25	0.091	30	1.0	0.022	8.479	0.969	1.682
M6	27	3.25	0.091	60	1.0	0.025	7.700	0.950	1.625
M6	28	3.25	0.091	90	1.0	0.005	42.678	1.006	1.415
M7	29	3.25	0.091	0	1.0	0.004	3616.659	0.992	1.627
M7	30	3.25	0.091	30	1.0	0.014	8.465	1.005	1.598
M7	31	3.25	0.091	60	1.0	0.020	7.206	0.956	1.574
M7	32	3.25	0.091	90	1.0	0.003	43.884	0.991	1.380
M8	33	3.7	0.2	0	1.0	0.060	2253.268	1.017	2.111
M8	34	3.7	0.2	30	1.0	0.116	4.867	0.867	2.410
M8	35	3.7	0.2	60	1.0	0.044	3.583	0.794	2.435
M8	36	3.7	0.2	90	1.0	0.031	6.958	0.668	2.573
M9	37	4.23	0.301	0	1.0	0.223	3693.041	0.941	2.816
M9	38	4.23	0.301	30	1.0	0.157	3.996	0.826	3.040
M9	39	4.23	0.301	60	1.0	0.041	3.755	0.636	3.785
M9	40	4.23	0.301	90	1.0	0.033	6.002	0.452	5.012

Table S.8: Additional list of parameters for the models M0-M9 (see Table S.1). VMF is the vapor mass fraction, T_{spin} is the spin orbital period in hours, I_z and I_x are the moments of inertia along z and x , respectively. The last column I_z is normalized by 10^{37} kg m².

Run	ID	M_T	γ	θ	$\frac{v_{\text{imp}}}{v_{\text{esc}}}$	VMF	T_{spin} (hrs)	I_x/I_z	$I_z \times 10^{-37}$
M10	41	5.34	0.091	0	1.0	0.021	2349.659	1.200	3.494
M10	42	5.34	0.091	30	1.0	0.081	8.559	0.955	3.759
M10	43	5.34	0.091	60	1.0	0.009	20.835	0.707	4.379
M10	44	5.34	0.091	90	1.0	0.010	41.717	0.989	3.075
M11	45	6.54	0.091	0	1.0	0.040	2340.101	0.851	5.231
M11	46	6.54	0.091	30	1.0	0.124	8.498	0.968	5.219
M11	47	6.54	0.091	60	1.0	0.013	20.168	0.780	5.490
M11	48	6.54	0.091	90	1.0	0.013	38.829	0.995	4.222
M12	49	8.94	0.091	0	1.0	0.187	394.894	1.251	8.647
M12	50	8.94	0.091	30	1.0	0.268	5.980	1.140	9.114
M12	51	8.94	0.091	60	1.0	0.036	14.045	1.016	7.045
M12	52	8.94	0.091	90	1.0	0.032	42.282	0.996	6.885
M13	53	9.43	0.104	0	1.0	0.247	1080.059	0.997	9.087
M13	54	9.43	0.104	30	1.0	0.279	6.502	0.947	9.311
M13	55	9.43	0.104	60	1.0	0.173	6.154	0.945	8.870
M13	56	9.43	0.104	90	1.0	0.033	31.994	0.954	7.626
M14	57	26.84	0.091	0	1.0	0.770	5883.023	1.000	43.983
M14	58	26.84	0.091	30	1.0	0.502	6.912	0.962	44.757
M14	59	26.84	0.091	60	1.0	0.192	10.440	0.984	42.126
M14	60	26.84	0.091	90	1.0	0.064	31.166	0.999	37.065
M15	61	53.66	0.091	0	1.0	0.964	9109.850	0.995	127.215
M15	62	53.66	0.091	30	1.0	0.757	6.418	0.959	129.038
M15	63	53.66	0.091	60	1.0	0.309	9.732	0.956	113.856
M15	64	53.66	0.091	90	1.0	0.101	30.287	0.997	106.793

Table S.9: Additional list of parameters for the models M10-M15 (see Table S.2).

Run	ID	M_T	γ	θ	$\frac{v_{\text{imp}}}{v_{\text{esc}}}$	VMF	T_{spin} (hrs)	I_x/I_z	$I_z \times 10^{-37}$
M16	65	1.88	0.5	0	1.3	0.180	4627.804	1.090	0.659
M16	66	1.88	0.5	30	1.3	0.060	4.045	0.637	1.378
M16	67	1.88	0.5	60	1.3	0.002	8.878	0.981	0.222
M16	68	1.88	0.5	90	1.3	0.000	13.381	1.007	0.221
M17	69	3.25	0.091	0	1.1	0.015	4302.774	0.944	1.711
M17	70	3.25	0.091	30	1.1	0.029	8.170	0.964	1.683
M17	71	3.25	0.091	60	1.1	0.005	20.271	1.003	1.427
M17	72	3.25	0.091	90	1.1	0.001	77.743	0.997	1.387
M18	73	3.25	0.091	0	1.2	0.021	7074.261	1.060	1.640
M18	74	3.25	0.091	30	1.2	0.034	7.969	0.972	1.657
M18	75	3.25	0.091	60	1.2	0.005	21.785	0.993	1.419
M18	76	3.25	0.091	90	1.2	0.001	76.341	0.998	1.383
M19	77	3.25	0.091	0	1.3	0.034	8587.565	1.119	1.643
M19	78	3.25	0.091	30	1.3	0.041	7.952	0.955	1.657
M19	79	3.25	0.091	60	1.3	0.007	26.404	0.998	1.394
M19	80	3.25	0.091	90	1.3	0.001	201.755	0.998	1.373
M20	81	3.25	0.091	0	1.4	0.044	2848.585	1.128	1.671
M20	82	3.25	0.091	30	1.4	0.052	8.227	1.138	1.655
M20	83	3.25	0.091	60	1.4	0.006	25.944	0.997	1.398
M20	84	3.25	0.091	90	1.4	0.001	284.157	1.000	1.376
M21	85	3.25	0.091	0	1.5	0.056	6608.636	1.057	1.665
M21	86	3.25	0.091	30	1.5	0.062	7.714	0.994	1.639
M21	87	3.25	0.091	60	1.5	0.008	32.555	0.997	1.396
M21	88	3.25	0.091	90	1.5	0.001	400.109	0.997	1.376
M22	89	3.25	0.091	0	2.0	0.340	3269.097	1.081	1.719
M22	90	3.25	0.091	30	2.0	0.106	10.451	0.965	1.524
M22	91	3.25	0.091	60	2.0	0.008	64.683	1.005	1.395
M22	92	3.25	0.091	90	2.0	0.000	44.092	1.000	1.383
M23	93	4.23	0.301	0	1.1	0.214	1939.650	0.715	3.083
M23	94	4.23	0.301	30	1.1	0.203	4.142	0.811	3.134
M23	95	4.23	0.301	60	1.1	0.010	11.238	0.987	1.454
M23	96	4.23	0.301	90	1.1	0.003	18.179	0.979	1.401
M24	97	4.23	0.301	0	1.2	0.290	2915.583	1.374	2.471
M24	98	4.23	0.301	30	1.2	0.231	4.195	0.859	2.989
M24	99	4.23	0.301	60	1.2	0.008	19.433	1.073	1.406
M24	100	4.23	0.301	90	1.2	0.002	136.449	1.007	1.383
M25	101	4.23	0.301	0	1.3	0.436	1589.596	0.870	2.845
M25	102	4.23	0.301	30	1.3	0.313	4.875	0.753	3.678
M25	103	4.23	0.301	60	1.3	0.010	19.620	1.103	1.407
M25	104	4.23	0.301	90	1.3	0.002	879.278	1.012	1.392
M26	105	4.23	0.301	0	1.6	0.571	1295.750	0.720	2.661
M26	106	4.23	0.301	30	1.6	0.179	20.967	0.985	2.230
M26	107	4.23	0.301	60	1.6	0.012	15.578	0.963	1.421
M26	108	4.23	0.301	90	1.6	0.002	419.454	1.008	1.389

Table S.10: Additional list of parameters for the models M16-M26 (see Table S.3).